

An efficient compact splitting Fourier spectral methods for computing the dynamics of rotating spin-orbit coupled spin-2 Bose-Einstein condensates

Xin Liu^a, Ziqing Xie^b, Yongjun Yuan^b, Yong Zhang^{c,d}, Xinyi Zhao^{b,*}

^a*Eastern Institute for Advanced Study, Eastern Institute of Technology, Ningbo, 315200, China*

^b*MOE-LCSM, School of Mathematics and Statistics, Hunan Normal University, Changsha, Hunan 410081, China*

^c*Center for Applied Mathematics and KL-AAGDM, Tianjin University, Tianjin, 300072, China*

^d*State Key Laboratory of Synthetic Biology, Tianjin University, Tianjin, 300072, China*

Abstract

This paper investigates the dynamics of spin-2 Bose-Einstein condensates (BECs) with rotation and spin-orbit coupling (SOC). In order to better simulate the dynamics, we present an efficient high-order compact splitting Fourier spectral method. This method splits the Hamiltonian into a linear part, which consists of the Laplace, rotation and SOC terms, and a nonlinear part that includes all the remaining terms. The wave function is well approximated by the Fourier spectral method and is numerically accessed with discrete Fast Fourier transform (FFT). For linear subproblem, the handling of rotation term and SOC term poses a major challenge. Using a function mapping based on rotation, we can integrate the linear subproblem exactly and explicitly. This mapping we propose not only helps eliminate the rotation term, but also prevents the SOC term from evolving into a time-dependent form. The nonlinear subproblem is integrated analytically in physical space. Such “compact” splitting involves only two operators and facilitates the design of high-order splitting schemes. Our method is spectrally accurate in space and high order in time. It is efficient, explicit, unconditionally stable and simple to implement. In addition, we derive some dynamical properties and carry out a systematic study, including accuracy and efficiency tests, dynamical property verification, the SOC effects and dynamics of vortex lattice.

Keywords: Spin-2 Bose-Einstein condensates, spin-orbit coupling, rotating, dynamic, Time splitting method, Fourier spectral method.

Contents

1	Introduction	2
2	Dynamical properties	4
3	Numerical methods	8
3.1	Exact integrator for Laplace-Rotation-SOC subproblem	8
3.2	Exact evaluation for nonlinear subproblem	11
3.3	High-order compact splitting Fourier spectral method	12
3.4	Stability	13

*Corresponding author.

Email addresses: xinliu@eitech.edu.cn (Xin Liu), ziqingxie@hunnu.edu.cn (Ziqing Xie), yyj1983@hunnu.edu.cn (Yongjun Yuan), Zhang_Yong@tju.edu.cn (Yong Zhang), xinyizhao@hunnu.edu.cn (Xinyi Zhao)

4 Numerical results	14
4.1 Accuracy confirmation	14
4.2 Efficiency test	16
4.3 Dynamical properties verification	17
4.4 SOC effects	18
4.5 Dynamics of a vortex lattice	18
5 Conclusion	19

1. Introduction

Bose-Einstein condensate (BEC) is a gaseous, superfluid state of matter that forms when the dilute boson gas is cooled to temperatures near absolute zero. In 1995, a team led by Eric Cornell and Carl Wieman combined laser and evaporative cooling techniques to achieve the first observation of BEC in the dilute ^{87}Rb gases [1]. Early experiments used magnetic traps, which froze the spin degrees of the atoms. In 1998, a BEC with internal spin degrees of freedom, known as a spinor BEC, was first realized in an optical dipole trap [26]. In optical traps, due to the interparticle interaction, the direction of atomic spins can change. Consequently, the order parameter of a spin- F BEC has $2F + 1$ components, which can vary in space and time, giving rise to rich spin textures. Recently, the spin-orbit coupling (SOC), which plays a key role in spintronic devices [19], spin Hall effect [16], topological insulators [14] and Majorana fermions [31], has been successfully induced in a neutral atomic BECs by dressing two atomic spin states with a pair of lasers. These experiments sparked a strong activity in the area of spin-orbit-coupled cold atoms and discovered a number of exciting phenomena. In particular, many investigations show that the combination of SOC, rotation and atomic intrinsic interactions can generate various phenomena in the spinor BEC [15, 20, 35]. For example, a variety of exotic spin textures and fractional quantized vortices are exhibited for rotating spin-orbit-coupled BECs [36], a new necklace-type state with double-ring structure is created in a spin-1 BEC system due to the SOC and rotation, and the ground-state phase diagrams of the spin-orbit-angular-momentum coupled ^{87}Rb condensate are experimentally mapped out with first-order phase transitions [34], SOC can control topological vortical phase transitions characterized by Anderson-Toulouse vortices, vortex-dipole lattices, and perpendicular vortex chains in the ground states of spin-2 BEC with SOC and rotation [37].

In the mean-field regime, when the temperature T is much lower than the critical temperature T_c , a rotating SOC spin-2 BEC can be described by the five-component wave functions $\Psi := \Psi(\mathbf{x}, t) = (\psi_2(\mathbf{x}, t), \psi_1(\mathbf{x}, t), \psi_0(\mathbf{x}, t), \psi_{-1}(\mathbf{x}, t), \psi_{-2}(\mathbf{x}, t))^T$ satisfying the coupled Gross-Pitaevskii equations (CGPEs) [23, 30, 32]

$$i\partial_t\psi_{\pm 2} = \mathcal{H}_0\psi_{\pm 2} + \pm 2c_1F_z\psi_{\pm 2} + c_1F_{\mp}\psi_{\pm 1} + \frac{c_2}{\sqrt{5}}A_{00}\bar{\psi}_{\mp 2} - \gamma L_{\mp}\psi_{\pm 1}, \quad (1.1)$$

$$i\partial_t\psi_{\pm 1} = \mathcal{H}_0\psi_{\pm 1} + \pm c_1F_z\psi_{\pm 1} + c_1\left(\frac{\sqrt{6}}{2}F_{\mp}\psi_0 + F_{\pm}\psi_{\pm 2}\right) - \frac{c_2}{\sqrt{5}}A_{00}\bar{\psi}_{\mp 1} - \gamma[L_{\pm}\psi_{\pm 2} + \frac{\sqrt{6}}{2}L_{\mp}\psi_0], \quad (1.2)$$

$$i\partial_t\psi_0 = \mathcal{H}_0\psi_0 + \frac{\sqrt{6}}{2}c_1(F_+\psi_1 + F_-\psi_{-1}) + \frac{c_2}{\sqrt{5}}A_{00}\bar{\psi}_0 - \frac{\sqrt{6}}{2}\gamma[L_+\psi_1 + L_-\psi_{-1}], \quad (1.3)$$

where $\mathcal{H}_0 = (-\frac{1}{2}\Delta + V + c_0\rho - \Omega L_z)$. Here t denotes time and $\mathbf{x} = (x, y)^T \in \mathbb{R}^2$ or $\mathbf{x} = (x, y, z)^T \in \mathbb{R}^3$ is the Cartesian coordinate vector. \bar{f} represents the conjugate of complex number f . c_0 , c_1 and c_2 are the dimensionless mean-field, spin-exchange interaction constant and spin singlet-pairing interaction constants respectively. Δ is the Laplacian operator, and $\rho = \sum_{\ell=-2}^2 |\psi_{\ell}|^2$ is the total density. The constant Ω is the angular velocity, and $L_z = -i(x\partial_y - y\partial_x)$ is the z-component of the angular momentum operator. The constant γ is the coupling strength, and $L_{\pm} := i\partial_y \pm \partial_x$ are the spin-orbit coupling operators. $V = V(\mathbf{x})$ is

a real-valued external trapping potential. Here we choose $V(\mathbf{x})$ as a harmonic potential, i.e.,

$$V(\mathbf{x}) = \frac{1}{2} \begin{cases} \gamma_x^2 x^2 + \gamma_y^2 y^2, & d = 2, \\ \gamma_x^2 x^2 + \gamma_y^2 y^2 + \gamma_z^2 z^2, & d = 3, \end{cases} \quad (1.4)$$

where γ_x , γ_y , and γ_z represent the trap frequencies in the respective x -, y -, and z -directions. The spin vector $\mathbf{F} := (F_x(\Psi), F_y(\Psi), F_z(\Psi))^\top := (\Psi^\mathbf{H} f_x \Psi, \Psi^\mathbf{H} f_y \Psi, \Psi^\mathbf{H} f_z \Psi)^\top$ with the conjugate transpose $\Psi^\mathbf{H}$ of Ψ and the spin-2 matrices $\mathbf{f} = (f_x, f_y, f_z)^\top$, where

$$f_x = \begin{pmatrix} 0 & 1 & 0 & 0 & 0 \\ 1 & 0 & \frac{\sqrt{6}}{2} & 0 & 0 \\ 0 & \frac{\sqrt{6}}{2} & 0 & \frac{\sqrt{6}}{2} & 0 \\ 0 & 0 & \frac{\sqrt{6}}{2} & 0 & 1 \\ 0 & 0 & 0 & 1 & 0 \end{pmatrix}, f_y = i \begin{pmatrix} 0 & -1 & 0 & 0 & 0 \\ 1 & 0 & -\frac{\sqrt{6}}{2} & 0 & 0 \\ 0 & \frac{\sqrt{6}}{2} & 0 & -\frac{\sqrt{6}}{2} & 0 \\ 0 & 0 & \frac{\sqrt{6}}{2} & 0 & -1 \\ 0 & 0 & 0 & 1 & 0 \end{pmatrix}, f_z = \begin{pmatrix} 2 & 0 & 0 & 0 & 0 \\ 0 & 1 & 0 & 0 & 0 \\ 0 & 0 & 0 & 0 & 0 \\ 0 & 0 & 0 & -1 & 0 \\ 0 & 0 & 0 & 0 & -2 \end{pmatrix}.$$

Furthermore, $A_{00} := \Psi^\mathbf{T} A \Psi$ with the matrix A taking the form $A_{ij} = \frac{1}{\sqrt{5}} (-1)^{i-1} \delta_{i+j,6}$ ($i, j = 1, 2, \dots, 5$), where $\delta_{i+j,6}$ represents the Kronecker delta. To be more detailed, we have

$$\begin{aligned} F_x &= \bar{\psi}_1 \psi_2 + \bar{\psi}_2 \psi_1 + \bar{\psi}_{-2} \psi_{-1} + \bar{\psi}_{-1} \psi_{-2} + \frac{\sqrt{6}}{2} (\bar{\psi}_0 \psi_1 + \bar{\psi}_1 \psi_0 + \bar{\psi}_{-1} \psi_0 + \bar{\psi}_0 \psi_{-1}), \\ F_y &= i \left[\bar{\psi}_1 \psi_2 - \bar{\psi}_2 \psi_1 + \bar{\psi}_{-2} \psi_{-1} - \bar{\psi}_{-1} \psi_{-2} + \frac{\sqrt{6}}{2} (\bar{\psi}_0 \psi_1 - \bar{\psi}_1 \psi_0 + \bar{\psi}_{-1} \psi_0 - \bar{\psi}_0 \psi_{-1}) \right], \\ F_z &= 2 |\psi_2|^2 + |\psi_1|^2 - |\psi_{-1}|^2 - 2 |\psi_{-2}|^2, \quad A_{00} = \frac{1}{\sqrt{5}} (2\psi_2 \psi_{-2} - 2\psi_1 \psi_{-1} + \psi_0^2). \end{aligned}$$

Notice that all spin-2 matrices are Hermitian and the spin vector entries are real numbers. The CGPEs (1.5) can be written in the compact form as

$$i\partial_t \Psi = (\mathcal{H}_0 I_5 + c_1 \mathbf{F} \cdot \mathbf{f} - \gamma \mathcal{S}) \Psi + c_2 A_{00} A \bar{\Psi}, \quad (1.5)$$

where I_5 is the 5×5 identity matrix and

$$\mathcal{S} = \begin{pmatrix} 0 & L_- & 0 & 0 & 0 \\ L_+ & 0 & \frac{\sqrt{6}}{2} L_- & 0 & 0 \\ 0 & \frac{\sqrt{6}}{2} L_+ & 0 & \frac{\sqrt{6}}{2} L_- & 0 \\ 0 & 0 & \frac{\sqrt{6}}{2} L_+ & 0 & L_- \\ 0 & 0 & 0 & L_+ & 0 \end{pmatrix}, \quad \mathbf{F} \cdot \mathbf{f} = \begin{pmatrix} 2F_z & F_- & 0 & 0 & 0 \\ F_+ & F_z & \frac{\sqrt{6}}{2} F_- & 0 & 0 \\ 0 & \frac{\sqrt{6}}{2} F_+ & 0 & \frac{\sqrt{6}}{2} F_- & 0 \\ 0 & 0 & \frac{\sqrt{6}}{2} F_+ & -F_z & F_- \\ 0 & 0 & 0 & F_+ & -2F_z \end{pmatrix},$$

with $F_+ = F_x + iF_y = 2(\bar{\psi}_2 \psi_1 + \bar{\psi}_{-1} \psi_{-2}) + \sqrt{6}(\bar{\psi}_1 \psi_0 + \bar{\psi}_0 \psi_{-1})$ and $F_- = F_x - iF_y = \bar{F}_+$.

There have been many numerical methods proposed for studying the dynamics of single-component BEC [2, 3, 5, 8, 11, 24, 29], among which the time-splitting sine/Fourier pseudospectral method is one of the most successful. The time-splitting pseudospectral method exhibits spatial spectral-order accuracy and is relatively straightforward to implement. As far as we known, this method has been generalized to study the dynamics of spinor BECs [4], nonrotating/rotating spin-1 BEC with SOC term [9, 12, 17, 23], and nonrotating spin-2 BEC with SOC term [9]. There are little research on dynamic simulations for spin-2 BEC with SOC term and the more physically interesting rotating case. In this paper, we aim to perform a comprehensive study of the dynamics for rotating SOC spin-2 BEC.

Numerically, the most challenges lie in proper treatments of the rotation and SOC terms. There exist some methods that successfully handle the rotating term. The standard alternating direction implicit (standard ADI) method splits the Hamiltonian into three parts and is of second order accurate in time [7]. However, it is somewhat tedious and complicated to construct a high-order scheme with such triple

operators. The exact splitting method (ESM) groups the Laplace and rotation terms into a linear part, enabling its corresponding subproblem to be integrated analytically and explicitly in Fourier space [22]. This property facilitates the construction of high-order temporal schemes. However, extending or adapting ESM to spinor BEC with SOC term remains nontrivial and highly challenging. The rotating Lagrangian coordinates (RLC) method eliminates the rotation term, thus simplifying the construction of high-order schemes [6]. However, when real-time dynamics are required, it is imperative to rotate the wave function $\psi(\mathbf{x}, t)$ from rotating Lagrangian coordinates to physical Cartesian coordinates at each time step t_n , and such rotation mapping is quite exhaustive computationally and poses great challenges to the simulation efficiency. Under these circumstances, Liu et al. [23] proposed a method that not only borrows the RLC idea to handle the rotation term, but also effectively addresses the complexities introduced by the SOC term.

In [23], by rotating the wave function in a fixed rectangular domain, the rotational term is eliminated for the rotated wave function. However, the SOC term thereby becomes explicitly time-dependent. To handle this, the linear system is integrated in Fourier space via a complicated time-dependent matrix decomposition. Notably, Liu et al. proposed a Rotation-Shear-Decomposition-Acceleration (RSDA) method to implement the function-rotation, replacing the conventional Fourier spectral interpolation approach. The RSDA can reformulate the rotation mapping into a computationally friendly form by using three-shear decomposition of the rotation matrix and its equivalent PDE reformulation. Meanwhile, since RSDA can be implemented efficiently with one-dimensional FFT/iFFT in Fourier space, it results in a significant efficiency enhancement.

To efficiently simulate the dynamics of rotating SOC spin-2 BEC, we introduce a high-order compact splitting Fourier spectral method. To be specific, the CGPEs (1.5) is split into a linear subproblem

$$i\partial_t\Psi(\mathbf{x}, t) = \left[\left(-\frac{1}{2}\Delta - \Omega L_z\right)I_5 - \gamma\mathcal{S} \right] \Psi(\mathbf{x}, t) + c_2 A_{00} A\bar{\Psi}(\mathbf{x}, t) := \mathcal{A}\Psi(\mathbf{x}, t), \quad (1.6)$$

and a nonlinear subproblem

$$i\partial_t\Psi(\mathbf{x}, t) = [(V + c_0\rho)I_5 + c_1\mathbf{F} \cdot \mathbf{f}] \Psi(\mathbf{x}, t) + c_2 A_{00} A\bar{\Psi}(\mathbf{x}, t) := \mathcal{B}\Psi(\mathbf{x}, t). \quad (1.7)$$

The nonlinear subproblem is integrated analytically in physical space. Inspired by the idea of [23], we propose a new function mapping that better addresses linear subproblem.

The function mapping proposed in the [23] turns SOC term into time-dependent, that brings difficulties to solving linear subproblem. Therefore, based on our observations, we propose in this paper a new function mapping (3.2). This mapping not only eliminates the rotational term but also prevents the SOC term from becoming time-dependent. Although it introduces an additional term, this term is completely explicit and linear, and thus poses no difficulty to the solution process.

The organization of this paper is as follows. In Section 2, we derive some dynamical laws for some physical quantities. In Section 3, we propose an efficient and robust splitting Fourier spectral method to simulate the dynamics, and prove the mass conservation (unconditionally stability) and magnetization conservation. In Section 4, we test the temporal/spatial accuracies and efficiency, and study some interesting numerical phenomena. We make some concluding remarks in Section 5.

2. Dynamical properties

In this section, we demonstrate some main quantities in the study of dynamics of spin-2 BEC with rotation and SOC, including mass, energy, magnetization, angular momentum expectation and condensate width. The dynamical laws of these quantities are briefly presented and can be used as benchmarks for testing our numerical methods.

Mass and energy. The CGPEs (1.5) have two important invariants: the mass of the wave function, which is defined as

$$\mathcal{N}(t) := \mathcal{N}(\Psi(\cdot, t)) := \int_{\mathbb{R}^d} \sum_{\ell=-2}^2 |\psi_\ell(\mathbf{x}, t)|^2 d\mathbf{x} \equiv \mathcal{N}(\Psi(\cdot, 0)) \equiv 1, \quad t \geq 0, \quad (2.1)$$

and the energy per particle

$$\begin{aligned}
\mathcal{E}(t) := \mathcal{E}(\Psi(\cdot, t)) &= \int_{\mathbb{R}^d} \sum_{\ell=-2}^2 \left(\frac{1}{2} |\nabla \psi_\ell|^2 + V(\mathbf{x}) |\psi_\ell|^2 - \Omega \bar{\psi}_\ell L_z \psi_\ell \right) + \frac{c_0}{2} \rho^2 + \frac{c_1}{2} (|F_+|^2 + |F_z|^2) \\
&+ \frac{c_2}{2} |A_{00}|^2 - \gamma \left[\bar{\psi}_2 L_- \psi_1 + \bar{\psi}_1 (L_+ \psi_2 + \frac{\sqrt{6}}{2} L_- \psi_0) + \frac{\sqrt{6}}{2} \bar{\psi}_0 (L_+ \psi_1 + L_- \psi_{-1}) \right. \\
&+ \left. \bar{\psi}_{-1} (L_- \psi_{-2} + \frac{\sqrt{6}}{2} L_+ \psi_0) + \bar{\psi}_{-2} L_+ \psi_{-1} \right] d\mathbf{x} \\
&\equiv \mathcal{E}(\Psi(\cdot, 0)).
\end{aligned} \tag{2.2}$$

Magnetization. The magnetization of the wave function, defined as

$$\mathcal{M}(t) = \mathcal{M}(\Psi(\cdot, t)) := \sum_{\ell=-2}^2 \int_{\mathbb{R}^d} \ell |\psi_\ell(\mathbf{x}, t)|^2 d\mathbf{x}, \tag{2.3}$$

satisfies the relation

$$\frac{d}{dt} \mathcal{M}(t) = 2\gamma \Re \int_{\mathbb{R}^d} i \left(\bar{\psi}_2 L_- \psi_1 - \psi_{-2} L_- \bar{\psi}_{-1} + \frac{\sqrt{6}}{2} \bar{\psi}_1 L_- \psi_0 - \frac{\sqrt{6}}{2} \psi_{-1} L_- \bar{\psi}_0 \right) d\mathbf{x}. \tag{2.4}$$

Thus the magnetization is conserved (i.e., $\mathcal{M}(t) \equiv \mathcal{M}(0)$, $t \geq 0$) in the absence of spin-orbit coupling ($\gamma = 0$).

Angular momentum expectation. The angular momentum expectation of the condensate (1.5) is defined as

$$\langle L_z \rangle(t) = \sum_{\ell=-2}^2 \int_{\mathbb{R}^d} \bar{\psi}_\ell(\mathbf{x}, t) L_z \psi_\ell(\mathbf{x}, t) d\mathbf{x}, \quad t \geq 0. \tag{2.5}$$

Lemma 1. For CGPEs (1.5) with harmonic potential (1.4), the dynamics of angular momentum expectation is governed by the following ordinary differential equation (ODE)

$$\frac{d\langle L_z \rangle(t)}{dt} = (\gamma_x^2 - \gamma_y^2) \int_{\mathbb{R}^d} xy \rho d\mathbf{x} - 2\gamma \Re \int_{\mathbb{R}^d} i \left(\bar{\psi}_{-1} L_- \psi_{-2} - \bar{\psi}_1 L_+ \psi_2 + \frac{\sqrt{6}}{2} \bar{\psi}_1 L_- \psi_0 - \frac{\sqrt{6}}{2} \bar{\psi}_{-1} L_+ \psi_0 \right) d\mathbf{x}.$$

Thus the angular momentum expectation is conserved, i.e.,

$$\langle L_z \rangle(t) \equiv \langle L_z \rangle(0), \quad t \geq 0, \tag{2.6}$$

when $\gamma_x = \gamma_y$ and $\gamma = 0$.

proof 1. By using (1.5) and performing integration by parts, we can derive

$$\begin{aligned}
\frac{d\langle L_z \rangle(t)}{dt} &= \sum_{\ell=-2}^2 \int [(\partial_t \bar{\psi}_\ell) (L_z \psi_\ell) + \bar{\psi}_\ell L_z (\partial_t \psi_\ell)] d\mathbf{x} \\
&= \int_{\mathbb{R}^d} V(\mathbf{x}) (x\partial_y - y\partial_x) \rho - \gamma i \left(\bar{\psi}_{-1} L_+ \bar{\psi}_2 + \bar{\psi}_{-1} L_- \psi_2 - \psi_1 L_- \bar{\psi}_2 - \psi_1 L_+ \bar{\psi}_2 \right. \\
&\quad \left. + \frac{\sqrt{6}}{2} [\psi_1 L_+ \bar{\psi}_0 + \bar{\psi}_1 L_- \psi_0 - \psi_{-1} L_- \psi_0 - \psi_{-1} L_+ \psi_0] \right) d\mathbf{x} \\
&= (\gamma_x^2 - \gamma_y^2) \int_{\mathbb{R}^d} xy \rho d\mathbf{x} - 2\gamma \Re \int_{\mathbb{R}^d} i \left(\bar{\psi}_{-1} L_- \psi_{-2} - \bar{\psi}_1 L_+ \psi_2 + \frac{\sqrt{6}}{2} \bar{\psi}_1 L_- \psi_0 - \frac{\sqrt{6}}{2} \bar{\psi}_{-1} L_+ \psi_0 \right) d\mathbf{x}.
\end{aligned}$$

This completes the proof.

Condensate width. The condensate width in the α -direction (where $\alpha = x, y, z$) is defined as $\sigma_\alpha = \sqrt{\delta_\alpha(t)}$, $t \geq 0$, where

$$\delta_\alpha(t) = \sum_{\ell=-2}^2 \delta_{\alpha,\ell}(t) \quad \text{with} \quad \delta_{\alpha,\ell} = \int_{\mathbb{R}^d} \alpha^2 |\psi_\ell(\mathbf{x}, t)|^2 d\mathbf{x}. \quad (2.7)$$

In particular, the following lemma describes its dynamics in the 2D case.

Lemma 2. For the 2D CGPEs (1.5) with the radially symmetric harmonic potential, i.e., (1.4) with $\gamma_x = \gamma_y =: \gamma_r$, we have

$$\frac{d^2 \delta_r(t)}{dt^2} = -4\gamma_r^2 \delta_r(t) + 4\mathcal{E}(0) + 4\Omega \langle L_z \rangle(t) + G(\gamma, \Psi), \quad (2.8)$$

where $\delta_r(t) := \delta_x(t) + \delta_y(t)$ and

$$\begin{aligned} G(\gamma, \Psi) = 2\gamma \Re \int_{\mathbb{R}^d} \Omega(iy - x) F_+ + \gamma \left(2\rho + 3|\psi_1|^2 + 4|\psi_0|^2 + 3|\psi_{-1}|^2 + 2\bar{\psi}_2 L_z \psi_2 + \bar{\psi}_1 L_z \psi_1 \right. \\ \left. - \bar{\psi}_{-1} L_z \psi_{-1} - 2\bar{\psi}_{-2} L_z \psi_{-2} \right) d\mathbf{x}. \end{aligned} \quad (2.9)$$

In particular, when $\gamma = 0$, it follows that

$$\delta_r(t) = \frac{\mathcal{E}(0) + \Omega \langle L_z \rangle(0)}{\gamma_r^2} [1 - \cos(2\gamma_r t)] + \delta_r^{(0)} \cos(2\gamma_r t) + \frac{\delta_r^{(1)}}{2\gamma_r} \sin(2\gamma_r t) \quad (2.10)$$

with $\delta_r^{(0)} = \delta_x(0) + \delta_y(0)$ and $\delta_r^{(1)} = \dot{\delta}_x(0) + \dot{\delta}_y(0)$. Furthermore, if the initial condition is radially symmetric, we have

$$\delta_x(t) = \delta_y(t) = \frac{1}{2} \delta_r(t), \quad t \geq 0.$$

Thus, the condensate widths $\sigma_x(t)$ and $\sigma_y(t)$ are periodic functions with frequency that is twice the trapping frequency γ_r in this case.

proof 2. By using (1.5), (2.7) and performing integration by parts, we can derive

$$\begin{aligned} \frac{d\delta_{\alpha,2}(t)}{dt} &= \int_{\mathbb{R}^d} \alpha^2 \partial_t |\psi_2|^2 d\mathbf{x} = \int_{\mathbb{R}^d} \alpha^2 (\partial_t \psi_2 \bar{\psi}_2 + \psi_2 \partial_t \bar{\psi}_2) d\mathbf{x} \\ &= 2\Re \int_{\mathbb{R}^d} i\alpha \left(\psi_2 \partial_\alpha \bar{\psi}_2 - \Omega |\psi_2|^2 L_z \alpha + c_1 \alpha F_+ \bar{\psi}_1 \psi_2 + \frac{c_2}{\sqrt{5}} \alpha \bar{A}_{00} \psi_{-2} \psi_2 + \gamma \alpha \psi_2 L_+ \bar{\psi}_1 \right) d\mathbf{x}. \end{aligned}$$

Analogously, we have

$$\begin{aligned} \frac{d\delta_{\alpha,\pm 1}(t)}{dt} &= 2\Re \int_{\mathbb{R}^d} i\alpha \left(\psi_{\pm 1} \partial_\alpha \bar{\psi}_{\pm 1} - \Omega |\psi_{\pm 1}|^2 L_z \alpha + c_1 \alpha \left[\frac{\sqrt{6}}{2} F_\pm \bar{\psi}_0 \psi_{\pm 1} + F_\mp \bar{\psi}_{\pm 2} \psi_{\pm 1} \right] - \frac{c_2}{\sqrt{5}} \alpha \bar{A}_{00} \psi_{\mp 1} \psi_{\pm 1} \right. \\ &\quad \left. + \gamma \alpha \left[\psi_{\pm 1} L_\mp \bar{\psi}_{\pm 2} + \frac{\sqrt{6}}{2} \psi_{\pm 1} L_\pm \bar{\psi}_0 \right] \right) d\mathbf{x}, \\ \frac{d\delta_{\alpha,0}(t)}{dt} &= 2\Re \int_{\mathbb{R}^d} i\alpha \left(\psi_0 \partial_\alpha \bar{\psi}_0 - \Omega |\psi_0|^2 L_z \alpha + \frac{\sqrt{6}}{2} c_1 \alpha \left[F_- \bar{\psi}_1 \psi_0 + F_+ \bar{\psi}_{-1} \psi_0 \right] + \frac{c_2}{\sqrt{5}} \alpha \bar{A}_{00} \psi_0^2 \right. \\ &\quad \left. + \frac{\sqrt{6}}{2} \gamma \alpha \left[\psi_0 L_- \bar{\psi}_1 + \psi_0 L_+ \bar{\psi}_{-1} \right] \right) d\mathbf{x}, \\ \frac{d\delta_{\alpha,-2}(t)}{dt} &= 2\Re \int_{\mathbb{R}^d} i\alpha \left(\psi_{-2} \partial_\alpha \bar{\psi}_{-2} - \Omega |\psi_{-2}|^2 L_z \alpha + c_1 \alpha F_- \bar{\psi}_{-1} \psi_{-2} + \frac{c_2}{\sqrt{5}} \alpha \bar{A}_{00} \psi_2 \psi_{-2} + \gamma \alpha \psi_{-2} L_- \bar{\psi}_{-1} \right) d\mathbf{x}. \end{aligned}$$

Then, a straightforward rearrangement shows

$$\begin{aligned} \frac{d\delta_\alpha(t)}{dt} &= \sum_{\ell=-2}^2 \frac{d\delta_{\alpha,\ell}(t)}{dt} = 2\Re \int_{\mathbb{R}^d} i\alpha \left(\sum_{\ell=-2}^2 (\psi_\ell \partial_\alpha \bar{\psi}_\ell - \Omega |\psi_\ell|^2 L_z \alpha) + \gamma \alpha \left[\bar{\psi}_2 L_- \psi_1 + \psi_1 L_- \bar{\psi}_2 + \bar{\psi}_{-1} L_- \psi_{-2} \right. \right. \\ &\quad \left. \left. + \psi_{-2} L_- \bar{\psi}_{-1} + \frac{\sqrt{6}}{2} (\bar{\psi}_1 L_- \psi_0 + \psi_0 L_- \bar{\psi}_1 + \bar{\psi}_0 L_- \psi_{-1} + \psi_{-1} L_- \bar{\psi}_0) \right] \right) dx. \end{aligned}$$

By performing integration by parts, we have

$$2\Re \int_{\mathbb{R}^d} i\gamma \alpha^2 \psi_1 L_- \bar{\psi}_2 dx = -2\Re \int_{\mathbb{R}^d} i\gamma \bar{\psi}_2 L_- (\alpha^2 \psi_1) dx = -2\Re \int_{\mathbb{R}^d} i\gamma (\alpha^2 \bar{\psi}_2 L_- \psi_1 + 2\alpha \bar{\psi}_2 \psi_1 L_- \alpha) dx.$$

Hence,

$$\begin{aligned} \frac{d\delta_\alpha(t)}{dt} &= 2\Re \int_{\mathbb{R}^d} i\alpha \left[\sum_{\ell=-2}^2 (\psi_\ell \partial_\alpha \bar{\psi}_\ell - \Omega |\psi_\ell|^2 L_z \alpha) - \gamma (2\bar{\psi}_2 \psi_1 L_- \alpha + 2\bar{\psi}_{-1} \psi_{-2} L_- \alpha + \sqrt{6} \bar{\psi}_1 \psi_0 L_- \alpha \right. \\ &\quad \left. + \sqrt{6} \bar{\psi}_0 \psi_{-1} L_- \alpha) \right] dx. \end{aligned}$$

By further differentiating the above equation with respect to t and suppressing the elementary but tedious computations, we obtain

$$\begin{aligned} \frac{d^2\delta_\alpha(t)}{dt^2} &= -2\gamma_r^2 \delta_\alpha(t) + \int_{\mathbb{R}^d} 2 \sum_{\ell=-2}^2 |\partial_\alpha \psi_\ell|^2 + c_0 \rho^2 + c_1 |F_z|^2 + c_1 |F_+|^2 + c_2 |A_{00}|^2 - 2\gamma (\bar{\psi}_2 L_- \psi_1 \\ &\quad + \bar{\psi}_1 (L_+ \psi_2 + \frac{\sqrt{6}}{2} L_- \psi_0) + \frac{\sqrt{6}}{2} \bar{\psi}_0 (L_+ \psi_1 + L_- \psi_{-1}) + \bar{\psi}_{-1} (L_- \psi_{-2} + \frac{\sqrt{6}}{2} L_+ \psi_0) + \bar{\psi}_{-2} L_+ \psi_{-1}) \\ &\quad + 2\Omega (\partial_y - \partial_x) \alpha \left(2i \sum_{\ell=-2}^2 (\bar{\psi}_\ell (x\partial_y + y\partial_x) \psi_\ell) + \Omega (x^2 - y^2) \rho - \gamma (xF_x - yF_y) \right) dx + G_1(\alpha, \gamma, \Psi), \end{aligned} \tag{2.11}$$

where

$$\begin{aligned} G_1(\alpha, \gamma, \Psi) &= 2\gamma \Re \int_{\mathbb{R}^d} 2\alpha \left(L_+ \bar{\psi}_1 \partial_\alpha \psi_2 + (L_- \bar{\psi}_2 + \frac{\sqrt{6}}{2} L_+ \bar{\psi}_0) \partial_\alpha \psi_1 + \frac{\sqrt{6}}{2} (L_- \bar{\psi}_1 + L_+ \bar{\psi}_{-1}) \partial_\alpha \psi_0 \right. \\ &\quad + (L_+ \bar{\psi}_{-2} + \frac{\sqrt{6}}{2} L_- \bar{\psi}_0) \partial_\alpha \psi_{-1} + L_- \bar{\psi}_{-1} \partial_\alpha \psi_{-2} \left. \right) + L_- \alpha \left(2\psi_1 \partial_\alpha \bar{\psi}_2 + 2\psi_{-2} \partial_\alpha \bar{\psi}_{-1} + \sqrt{6} \psi_0 \partial_\alpha \bar{\psi}_1 \right. \\ &\quad + \sqrt{6} \psi_{-1} \partial_\alpha \bar{\psi}_0 - \Omega F_+ L_z \alpha + \gamma \left[2\alpha \bar{\psi}_2 L_+ \psi_2 + \alpha \bar{\psi}_1 L_+ \psi_1 + \alpha \psi_{-1} L_+ \bar{\psi}_{-1} + 2\alpha \psi_{-2} L_+ \bar{\psi}_{-2} \right. \\ &\quad \left. \left. - (2|\psi_1|^2 + 3|\psi_0|^2 + 2|\psi_{-1}|^2) L_+ \alpha - (\sqrt{6} \psi_0 \bar{\psi}_2 + 3\psi_{-1} \bar{\psi}_1 + \sqrt{6} \psi_{-2} \bar{\psi}_0) L_- \alpha \right] \right) dx. \end{aligned}$$

Hence, we have

$$\frac{d^2\delta_r(t)}{dt^2} = -4\gamma_r^2 \delta_r(t) + 4\mathcal{E}(\Psi(\cdot, 0)) + 4\Omega \langle L_z \rangle(t) + G(\gamma, \Psi),$$

where

$$\begin{aligned} G(\gamma, \Psi) &:= G_1(x, \gamma, \Psi) + G_1(y, \gamma, \Psi) \\ &= 2\gamma \int_{\mathbb{R}^d} -\Omega (xF_x + yF_y) + \gamma \left(2\rho + 3|\psi_1|^2 + 4|\psi_0|^2 + 3|\psi_{-1}|^2 + \sum_{\ell=-2}^2 \ell \bar{\psi}_\ell L_z \psi_\ell \right) dx. \end{aligned}$$

As a result, we have $G(0, \Psi) = 0$ and $\langle L_z \rangle(t) \equiv \langle L_z \rangle(0)$ when $\gamma = 0$. Consequently, the $\delta_r(t)$ given in (2.10) is the unique solution to second order ODE (2.8) with the initial data $\delta_r(0) = \delta_r^{(0)}$ and $\dot{\delta}_r(0) = \delta_r^{(1)}$. Furthermore, if $\Psi^0(\mathbf{x})$ is radial symmetric, the solution $\Psi(\mathbf{x}, t)$ is also radial symmetric since $\gamma_x = \gamma_y$, which implies that

$$\delta_x(t) = \delta_y(t) = \frac{1}{2}\delta_r(t), \quad t \geq 0.$$

This completes the proof.

3. Numerical methods

In this section, we develop a high-order compact splitting Fourier spectral method, where the Hamiltonian is split into a linear part \mathcal{A} (comprising the Laplace, rotation, and SOC terms) and a nonlinear part \mathcal{B} (consisting of all remaining terms). Each subproblem can be integrated exactly in phase or physical space, as detailed in Subsection 3.1 for the linear subproblem and in Subsection 3.2 for the nonlinear one.

3.1. Exact integrator for Laplace-Rotation-SOC subproblem

In this subsection, we propose an exact and efficient integrator to solve the following Laplace-Rotation-SOC subproblem

$$\begin{cases} i\partial_t \Psi(\mathbf{x}, t) = \left[\left(-\frac{1}{2}\Delta - \Omega L_z \right) I_5 - \gamma \mathcal{S} \right] \Psi(\mathbf{x}, t) := \mathcal{A}\Psi(\mathbf{x}, t), & t_n \leq t \leq t_{n+1}, \\ \Psi(\mathbf{x}, t_n) = \Psi^n, & \mathbf{x} \in \mathbb{R}^d. \end{cases} \quad (3.1)$$

Inspired by [23], we observe that, for the rotated wave function obtained by introducing a function-rotation mapping through a rotation of variables, the rotation term vanishes and the Laplace keeps unchanged, but the SOC term becomes time-dependent. This transformation removes the numerical challenge induced by the rotation term, but the time-dependent SOC term makes the resulting variable-coefficient ODE system difficult to calculate exactly. To address this issue, we introduce a **function-rotation mapping with a phase factor** defined as

$$\phi_\ell(\mathbf{x}, t) := e^{-i\ell\Omega t} \psi_\ell(\mathcal{R}(t)\mathbf{x}, t), \quad \mathbf{x} \in \mathbb{R}^d, \quad (3.2)$$

where $\mathcal{R}(t)$ is a time-dependent rotation matrix, given by

$$\mathcal{R}(t) = \begin{pmatrix} \cos(\Omega t) & \sin(\Omega t) \\ -\sin(\Omega t) & \cos(\Omega t) \end{pmatrix}, \quad \text{if } d = 2, \quad \mathcal{R}(t) = \begin{pmatrix} \cos(\Omega t) & \sin(\Omega t) & 0 \\ -\sin(\Omega t) & \cos(\Omega t) & 0 \\ 0 & 0 & 1 \end{pmatrix}, \quad \text{if } d = 3.$$

Using the chain rule, we obtain

$$\begin{aligned} \partial_t \phi_\ell(\mathbf{x}, t) &= -i\ell\Omega e^{-i\ell\Omega t} \psi_\ell(\tilde{\mathbf{x}}, t) + e^{-i\ell\Omega t} [\partial_t \psi_\ell(\tilde{\mathbf{x}}, t) - i\Omega L_z \psi_\ell(\tilde{\mathbf{x}}, t)], \quad \Delta \psi_\ell(\tilde{\mathbf{x}}, t) = e^{i\ell\Omega t} \Delta \phi_\ell(\mathbf{x}, t), \\ L_+ \psi_\ell(\tilde{\mathbf{x}}, t) &= e^{i\ell\Omega t} [i(-\sin(\Omega t)\partial_x + \cos(\Omega t)\partial_y) + (\cos(\Omega t)\partial_x + \sin(\Omega t)\partial_y)] \phi_\ell(\mathbf{x}, t) = e^{i(\ell-1)\Omega t} L_+ \phi_\ell(\mathbf{x}, t), \\ L_- \psi_\ell(\tilde{\mathbf{x}}, t) &= e^{i\ell\Omega t} [i(\cos(\Omega t)\partial_x + \sin(\Omega t)\partial_y) + (-\sin(\Omega t)\partial_x + \cos(\Omega t)\partial_y)] \phi_\ell(\mathbf{x}, t) = e^{i(\ell+1)\Omega t} L_- \phi_\ell(\mathbf{x}, t), \end{aligned}$$

where $\tilde{\mathbf{x}} := \mathcal{R}(t)\mathbf{x}$. From (3.1) and these relations, a simple derivation yields the following system for the vector $\Phi := (\phi_2, \phi_1, \phi_0, \phi_{-1}, \phi_{-2})^\top$.

$$\begin{cases} i\partial_t \Phi(\mathbf{x}, t) = \left[\left(-\frac{1}{2}\Delta\right)I_5 - \gamma\mathcal{S} + \Omega f_z \right] \Phi(\mathbf{x}, t) := \tilde{\mathcal{A}}\Phi(\mathbf{x}, t), & t_n \leq t \leq t_{n+1}, \\ \Phi(\mathbf{x}, t_n) = \Psi(\mathcal{R}(t_n)\mathbf{x}, t_n) := \Phi^n, & \mathbf{x} \in \mathbb{R}^d. \end{cases} \quad (3.3)$$

The Laplace and SOC terms remain unchanged, while the rotation term is eliminated and replaced by a constant term Ωf_z . Consequently, the resulting system becomes straightforward to integrate exactly in Fourier space.

Remark 3.1. *The introduction of a phase factor in the function-rotation mapping eliminates the time dependence of the coefficient matrix $\tilde{\mathcal{A}}$. In the absence of the phase factor [23], the SOC term becomes time-dependent, thereby destroying the constant-coefficient structure of the linear operator. With the phase factor included, the transformed system retains a time-invariant coefficient matrix $\tilde{\mathcal{A}} = \left(-\frac{1}{2}\Delta\right)I_5 - \gamma\mathcal{S} + \Omega f_z$ and thus admits exact integration in Fourier space.*

Since the wave function ψ_ℓ is smooth and decays exponentially fast, its mapped function ϕ_ℓ is also smooth and rapidly decaying. Therefore, it is reasonable to truncate the whole space \mathbb{R}^d into a common large enough bounded domain $\mathcal{D} = [-L, L]^d$, $L > 0$ and impose periodic boundary conditions for both ψ_ℓ and ϕ_ℓ . We then apply the Fourier spectral method [25] to approximate both wave functions and their spatial derivatives. For simplicity, we take 2D case as an example. The spatial mesh size is chosen as $h = 2L/N$ with $N \in 2\mathbb{Z}^+$. The Fourier, physical index and grid points sets are defined as follows

$$\begin{aligned} \mathcal{I}_N &= \{(j, k) \in \mathbb{Z}^2 \mid 0 \leq j \leq N-1, \ 0 \leq k \leq N-1\}, \\ \mathcal{T}_N &= \{(p, q) \in \mathbb{Z}^2 \mid -N/2 \leq p \leq N/2-1, \ -N/2 \leq q \leq N/2-1\}, \\ \mathcal{G} &= \{(x_j, y_k) := (-L + jh, -L + kh), \ (j, k) \in \mathcal{I}_N\}. \end{aligned}$$

In order to discrete (3.3), we approximate the function ϕ_ℓ by applying the Fourier spectral method

$$\phi_\ell(x, y, t) \approx \sum_{(p,q) \in \mathcal{T}_N} \hat{\phi}_{\ell,pq}(t) e^{i\nu_p(x+L)} e^{i\nu_q(y+L)}, \quad (x, y) \in \mathcal{D},$$

where $\nu_p = 2\pi p/(2L)$, $\nu_q = 2\pi q/(2L)$. The discrete Fourier coefficients are given by

$$\hat{\phi}_{\ell,pq}(t) \approx \frac{1}{N^2} \sum_{(j,k) \in \mathcal{I}_N} \phi_{\ell,jk}(t) e^{-i\nu_p(x_j+L)} e^{-i\nu_q(y_k+L)}, \quad (p, q) \in \mathcal{T}_N,$$

where $\phi_{\ell,jk}(t)$ is the numerical approximation of $\phi_\ell(x_j, y_k, t)$.

Applying the Fourier spectral approximation in space, the semi-discrete of (3.3) reduces to the following linear system for the Fourier coefficients

$$\begin{cases} i\partial_t \hat{\Phi}_{pq}(t) = \hat{\mathcal{A}} \hat{\Phi}_{pq}(t), & t_n \leq t \leq t_{n+1}, \\ \hat{\Phi}_{pq}(t_n) := (\hat{\Phi}^n)_{pq}, & (p, q) \in \mathcal{T}_N \end{cases} \quad (3.4)$$

with $\hat{\Phi}_{pq} := (\hat{\phi}_{2,pq}, \hat{\phi}_{1,pq}, \hat{\phi}_{0,pq}, \hat{\phi}_{-1,pq}, \hat{\phi}_{-2,pq})^\top$. The constant coefficient matrix is given by

$$\hat{\mathcal{A}} = \frac{1}{2}(\nu_p^2 + \nu_q^2)I_5 - \begin{pmatrix} -2\Omega & \gamma a & 0 & 0 & 0 \\ \gamma \bar{a} & -\Omega & \frac{\sqrt{6}}{2}\gamma a & 0 & 0 \\ 0 & \frac{\sqrt{6}}{2}\gamma \bar{a} & 0 & \frac{\sqrt{6}}{2}\gamma a & 0 \\ 0 & 0 & \frac{\sqrt{6}}{2}\gamma \bar{a} & \Omega & \gamma a \\ 0 & 0 & 0 & \gamma \bar{a} & 2\Omega \end{pmatrix} := \frac{1}{2}(\nu_p^2 + \nu_q^2)I_5 - Q$$

with $a := -\nu_q - i\nu_p$. The equation (3.4) is actually an ODE system with constant skew-Hermitian coefficient matrix, then we have

$$\widehat{\Phi}_{pq}(t) = e^{-i(t-t_n)\widehat{A}} (\widehat{\Phi}^n)_{pq} = e^{-\frac{1}{2}i(\nu_p^2 + \nu_q^2)(t-t_n)} e^{i(t-t_n)Q} (\widehat{\Phi}^n)_{pq}.$$

Therefore, the solution to system (3.3) at $t = t_{n+1}$ can be written as

$$\Phi_{jk}^{n+1} = \sum_{(p,q) \in \mathcal{T}_N} e^{-\frac{1}{2}i(\nu_p^2 + \nu_q^2)\tau} e^{i\tau Q} (\widehat{\Phi}^n)_{pq} e^{i\nu_p(x_j+L)} e^{i\nu_q(y_k+L)}. \quad (3.5)$$

Specifically, the matrix exponential $e^{i\tau Q}$ can be computed explicitly as

$$e^{i\tau Q} = \begin{pmatrix} c_{11} & ac_{12} & a^2c_{13} & a^3c_{14} & a^4c_{15} \\ \bar{a}c_{12} & c_{22} & ac_{23} & a^2c_{24} & a^3c_{25} \\ \bar{a}^2c_{13} & \bar{a}c_{23} & c_{33} & ac_{34} & a^2c_{35} \\ \bar{a}^3c_{14} & \bar{a}^2c_{24} & \bar{a}c_{34} & c_{44} & ac_{45} \\ \bar{a}^4c_{15} & \bar{a}^3c_{25} & \bar{a}^2c_{35} & \bar{a}c_{45} & c_{55} \end{pmatrix},$$

where

$$\begin{aligned} c_{11} &= \frac{1}{8\lambda^4} [(8\Omega^4 + 8\Omega^2\xi^2 + \xi^4)\eta_1 + 4\xi^2(2\Omega^2 + \xi^2)\eta_2 - 4\Omega\lambda(2\Omega^2 + \xi^2)\eta_3 - 8\Omega\lambda\xi^2\eta_4 + 8\lambda^4], \\ c_{12} &= \frac{\gamma}{4\lambda^4} [-\Omega(4\Omega^2 + 3\xi^2)\eta_1 + 4\Omega\xi^2\eta_2 + \lambda(4\Omega^2 + \xi^2)\eta_3 - 2\lambda(2\Omega^2 - \xi^2)\eta_4], \\ c_{13} &= \frac{\sqrt{6}\gamma^2}{4\lambda^4} [(2\Omega^2 + \xi^2)\eta_2 - 2\Omega\lambda\eta_4 + 2\lambda^2]\eta_2, \quad c_{14} = \frac{\gamma^3}{2\lambda^4} (-\Omega\eta_2 + \lambda\eta_4)\eta_2, \quad c_{15} = \frac{\gamma^4}{8\lambda^4} (\eta_1 - 4\eta_2), \\ c_{22} &= \frac{1}{2\lambda^4} (2\xi^2\eta_2 + \lambda^2) [(2\Omega^2 + \xi^2)\eta_2 - 2\Omega\lambda\eta_4 + 2\lambda^2], \quad c_{23} = \frac{\sqrt{6}\gamma}{2\lambda^4} (\xi^2\eta_2 + \lambda^2) (-\Omega\eta_2 + \lambda\eta_4), \\ c_{24} &= \frac{\gamma^2}{2\lambda^4} (2\xi^2\eta_2 + 3\lambda^2)\eta_2, \quad c_{25} = c_{14} + \frac{\Omega\gamma^3}{\lambda^4}\eta_2^2, \quad c_{33} = \frac{3\xi^2}{4\lambda^4} (\xi^2\eta_1 + 4\Omega^2\eta_2) + 1, \\ c_{34} &= c_{23} + \frac{\sqrt{6}\Omega\gamma}{\lambda^4} (\xi^2\eta_2 + \lambda^2)\eta_2, \quad c_{35} = c_{13} + \frac{\sqrt{6}\Omega\gamma^2}{\lambda^3}\eta_2\eta_4, \quad c_{44} = c_{22} + \frac{2\Omega}{\lambda^3} (2\xi^2\eta_2 + \lambda^2)\eta_4, \\ c_{45} &= c_{12} + \frac{\Omega\gamma}{2\lambda^4} [(4\Omega^2 + 3\xi^2)\eta_1 - 4\Omega^2\eta_2], \quad c_{55} = c_{11} + \frac{\Omega}{\lambda^3} [(2\Omega^2 + \xi^2)\eta_3 + 2\xi^2\eta_4] \end{aligned}$$

with $\xi = \gamma|a|$, $\lambda = \sqrt{\Omega^2 + \xi^2}$, $\eta_1 = \cos(2\lambda\tau) - 1$, $\eta_2 = \cos(\lambda\tau) - 1$, $\eta_3 = i \sin(2\lambda\tau)$, $\eta_4 = i \sin(\lambda\tau)$.

Remark 3.2. In fact, the matrix $e^{i\tau Q}$ depends only on Ω , γ and the time step τ , hence it can be computed once and treated as a pre-computation. This significantly reduces the computational cost compared with [23], where the corresponding matrix needs to be updated at each time step.

Finally, we obtain the solution to the linear subproblem (3.1) as

$$\psi_\ell^{n+1}(\mathbf{x}_{jk}) = e^{i\ell\Omega t} \phi_\ell^{n+1}(\mathcal{R}^{-1}(t_{n+1})\mathbf{x}_{jk}) \quad \text{with } \mathbf{x}_{jk} = (x_j, y_k)^\top.$$

To ensure that the proposed procedure is computationally viable, an efficient implementation of the function-rotation mapping with a phase factor is crucial. Fortunately, the inclusion of the phase factor does not introduce any additional computational difficulty, and the mapping can still be efficiently realized using the Rotation-Shear-Decomposition-Acceleration (RSDA) method [23]. Specifically,

$$\phi_\ell^n(\mathbf{x}) = e^{-i\ell\Omega t_n} e^{a_1 y \partial_x} e^{b_1 x \partial_y} e^{a_1 y \partial_x} \psi_\ell^n(\mathbf{x}), \quad \mathbf{x} \in \mathbb{R}^d, \quad (3.6)$$

$$\psi_\ell^{n+1}(\mathbf{x}) = e^{i\ell\Omega t_{n+1}} e^{a_2 y \partial_x} e^{b_2 x \partial_y} e^{a_2 y \partial_x} \phi_\ell^{n+1}(\mathbf{x}), \quad \mathbf{x} \in \mathbb{R}^d, \quad (3.7)$$

where $a_1 = \tan(\Omega t_n/2)$, $b_1 = -\sin(\Omega t_n)$, $a_2 = -\tan(\Omega t_{n+1}/2)$ and $b_2 = \sin(\Omega t_{n+1})$. The numerical implementation of (3.6) and (3.7) requires only one-dimensional FFTs and iFFTs, thereby achieving nearly optimal efficiency. Details can be found in [23].

Remark 3.3 (Special cases). *The proposed method naturally resolves special physical cases, such as the vanishing spin-orbit coupling case ($\gamma = 0$) and the non-rotating case ($\Omega = 0$).*

- **Non-SOC:** When the spin-orbit coupling strength γ goes to zero, we have

$$e^{i\tau Q} \rightarrow \begin{pmatrix} e^{-2i\tau\Omega} & 0 & 0 & 0 & 0 \\ 0 & e^{-i\tau\Omega} & 0 & 0 & 0 \\ 0 & 0 & 1 & 0 & 0 \\ 0 & 0 & 0 & e^{i\tau\Omega} & 0 \\ 0 & 0 & 0 & 0 & e^{2i\tau\Omega} \end{pmatrix} \quad (3.8)$$

and the numerical scheme (3.5) reads as

$$\phi_{\ell,jk}^{n+1} = \sum_{(p,q) \in \mathcal{T}_N} e^{-\frac{1}{2}i(\nu_p^2 + \nu_q^2)\tau} e^{-li\tau\Omega} (\widehat{\phi}_\ell^n)_{pq} e^{i\nu_p(x_j+L)} e^{i\nu_q(y_k+L)}.$$

This scheme aligns with the numerical scheme for solving the PDEs (3.1) with $\gamma = 0$ using the function-rotation mapping proposed in [23].

- **Non-rotating:** When the rotating speed Ω goes to zero, simple calculations imply that $\phi_\ell = \psi_\ell$ and $\widetilde{A} = (-\frac{1}{2}\Delta)I_5 - \gamma\mathcal{S} = \mathcal{A}$. Therefore, the corresponding numerical scheme aligns with the scheme for solving the PDEs (3.1) with $\Omega = 0$.

Remark 3.4 (Extension to three-dimensional problem). *It is straightforward to extend the above method to three dimensional case, because both the rotation and SOC terms are independent of space variable z , and we choose to omit details for brevity.*

3.2. Exact evaluation for nonlinear subproblem

In this subsection, we present an exact solution to the following nonlinear subproblem [27]

$$\begin{cases} i\partial_t \Psi(\mathbf{x}, t) = [(V(\mathbf{x}) + c_0\rho)I_5 + c_1\mathbf{F} \cdot \mathbf{f}] \Psi(\mathbf{x}, t) + c_2 A_{00} A \bar{\Psi}(\mathbf{x}, t), & t_n \leq t \leq t_{n+1}, \\ \Psi(\mathbf{x}, t_n) = \Psi^n, & \mathbf{x} \in \mathbb{R}^d, \end{cases} \quad (3.9)$$

where the nonlinearity arises only from the density $\rho = \Psi^H \Psi$, spin vector $\mathbf{F} = (F_x, F_y, F_z)^\top$ and $A_{00} = \Psi^\top A \Psi$. In fact, the above equation reduces to a linear ODE, since ρ and \mathbf{F} are time-independent and $A_{00}(t)$ can be solved analytically.

Specifically, using the facts that $f_\alpha(\alpha = x, y, z)$ and A are Hermitian matrices, and that the commutator relations $[f_x, f_y] := f_x f_y - f_y f_x = i f_z$, $[f_y, f_z] = i f_x$, $[f_z, f_x] = i f_y$ and $\Psi^\top A f_\alpha \Psi = 0$ hold, we have

$$\partial_t \rho = \partial_t (\Psi^H \Psi) = i c_1 \Psi^H ((\mathbf{F} \cdot \mathbf{f})^H - \mathbf{F} \cdot \mathbf{f}) \Psi + i c_2 \left(\overline{A_{00}} \Psi^\top A^H \Psi - A_{00} \Psi^H A \bar{\Psi} \right) = 0, \quad (3.10)$$

$$\partial_t F_\alpha = \partial_t (\Psi^H f_\alpha \Psi) = i c_1 \Psi^H [\mathbf{F} \cdot \mathbf{f}, f_\alpha] \Psi + i c_2 \left(\overline{A_{00}} \Psi^\top A f_\alpha \Psi - A_{00} \Psi^H f_\alpha A \bar{\Psi} \right) = 0. \quad (3.11)$$

This implies that ρ and F_α are time-invariant, i.e., $\rho(\mathbf{x}, t) \equiv \rho(\mathbf{x}, t_n) := \rho^n$ and $F_\alpha(\Psi) \equiv F_\alpha(\Psi^n) := F_\alpha^n$ for any time $t_n \leq t \leq t_{n+1}$. For the quantity A_{00} , using the identity $(\mathbf{F}^n \cdot \mathbf{f})A + A(\mathbf{F}^n \cdot \mathbf{f}) = 0$ with $\mathbf{F}^n := (F_x^n, F_y^n, F_z^n)^\top$, a simple calculation shows that

$$\partial_t A_{00} = -2i \left[V + \left(c_0 + \frac{c_2}{5} \right) \rho^n \right] A_{00},$$

from which we derive exact and explicit formula for the A_{00} as follows

$$A_{00}(t) = e^{-2i(t-t_n)} [V + (c_0 + \frac{c_2}{5})\rho^n] A_{00}^n \quad \text{with} \quad A_{00}^n = (\Psi^n)^\top A \Psi^n.$$

Introducing the transformation

$$\tilde{\Psi}(\mathbf{x}, t) := e^{i(t-t_n)} ([V + (c_0 + \frac{c_2}{5})\rho^n] I_5 + c_1 \mathbf{F}^n \cdot \mathbf{f}) \Psi(\mathbf{x}, t),$$

and plugging it into (3.9), we obtain

$$\partial_t \tilde{\Psi}(\mathbf{x}, t) = ic_2 \left(\frac{\rho^n}{5} \tilde{\Psi} - A_{00}^n A \tilde{\Psi} \right) \quad \text{with} \quad \tilde{\Psi}(\mathbf{x}, t_n) = \Psi^n. \quad (3.12)$$

To solve the ODE (3.12), we take its conjugate and introduce the vector $\zeta(\mathbf{x}, t) := (\tilde{\Psi}^\top, \bar{\tilde{\Psi}}^\top)^\top$, which satisfies

$$\partial_t \zeta(\mathbf{x}, t) = ic_2 \begin{pmatrix} \frac{\rho^n}{5} I_5 & -A_{00}^n A \\ \bar{A}_{00}^n A & -\frac{\rho^n}{5} I_5 \end{pmatrix} \zeta(\mathbf{x}, t) := ic_2 D \zeta(\mathbf{x}, t). \quad (3.13)$$

Clearly, the coefficient matrix D is time-independent and satisfies $D^2 = [(\rho^n/5)^2 - |A_{00}^n|^2/5] I_{10} := S^2 I_{10}$. It follows that the exact solution to ODE (3.13) reads as

$$\zeta(\mathbf{x}, t) = e^{ic_2(t-t_n)D} \zeta(\mathbf{x}, t_n) = \left[\cos(c_2 S(t-t_n)) I_{10} + \frac{i}{S} \sin(c_2 S(t-t_n)) D \right] \zeta(\mathbf{x}, t_n),$$

where $S = \sqrt{(\rho^n/5)^2 - |A_{00}^n|^2/5}$. Then we have

$$\tilde{\Psi}(\mathbf{x}, t) = \cos(c_2 S(t-t_n)) \Psi^n + \frac{i}{S} \sin(c_2 S(t-t_n)) \left(\frac{\rho^n}{5} \Psi^n - A_{00}^n A \bar{\Psi}^n \right).$$

Therefore, the exact solution to (3.9) reads as follows

$$\Psi(\mathbf{x}, t) = e^{-i(t-t_n)[V + (c_0 + c_2/5)\rho^n]} e^{-ic_1(t-t_n)\mathbf{F}^n \cdot \mathbf{f}} \left[\cos(c_2 S(t-t_n)) \Psi^n + \frac{i}{S} \sin(c_2 S(t-t_n)) \left(\frac{\rho^n}{5} \Psi^n - A_{00}^n A \bar{\Psi}^n \right) \right], \quad (3.14)$$

where $e^{-ic_1(t-t_n)\mathbf{F}^n \cdot \mathbf{f}}$ is calculated as

$$\begin{aligned} e^{-ic_1(t-t_n)\mathbf{F}^n \cdot \mathbf{f}} &= I_5 + i \left(\frac{1}{6} \sin(2\kappa) - \frac{4}{3} \sin(\kappa) \right) \frac{\mathbf{F}^n \cdot \mathbf{f}}{|\mathbf{F}^n|} + \left(\frac{4}{3} \cos(\kappa) - \frac{1}{12} \cos(2\kappa) - \frac{5}{4} \right) \frac{(\mathbf{F}^n \cdot \mathbf{f})^2}{|\mathbf{F}^n|^2} \\ &\quad + i \left(\frac{1}{3} \sin(\kappa) - \frac{1}{6} \sin(2\kappa) \right) \frac{(\mathbf{F}^n \cdot \mathbf{f})^3}{|\mathbf{F}^n|^3} + \left(\frac{1}{12} \cos(2\kappa) - \frac{1}{3} \cos(\kappa) + \frac{1}{4} \right) \frac{(\mathbf{F}^n \cdot \mathbf{f})^4}{|\mathbf{F}^n|^4} \end{aligned}$$

with $\kappa = c_1 |\mathbf{F}^n| (t-t_n)$.

3.3. High-order compact splitting Fourier spectral method

In this subsection, we construct high-order time marching schemes based on operator composition techniques. Let $\Psi(t) = e^{-i(t-t_n)\mathcal{A}} \Psi^n$ and $\Psi(t) = e^{-i(t-t_n)\mathcal{B}} \Psi^n$ denotes the solutions to linear subproblem and nonlinear subproblem respectively. In principle, high-order splitting schemes can be constructed as [33]

$$\Psi^{n+1} = \left(\prod_{j=1}^m e^{-ia_j \tau \mathcal{A}} e^{-ib_j \tau \mathcal{B}} \right) \Psi^n,$$

where the coefficients a_j and b_j ($j = 1, \dots, m$) are chosen properly. Here, we present two commonly used splitting schemes.

- **Second-order Strang splitting:** $m = 2$, $a_1 = a_2 = 1/2$, $b_1 = 1$, $b_2 = 0$,
- **Fourth-order symplectic time integrator:** $m = 4$, $a_1 = a_4 = \frac{1}{2(2-2^{1/3})}$, $a_2 = a_3 = \frac{1-2^{1/3}}{2(2-2^{1/3})}$,
 $b_1 = b_3 = \frac{1}{2-2^{1/3}}$, $b_2 = -\frac{2^{1/3}}{2-2^{1/3}}$, $b_4 = 0$.

In practice, from time $t = t_n$ to $t = t_{n+1}$, we combine the splitting steps via the standard Strang splitting and present detailed step-by-step algorithm in Algorithm 1.

Algorithm 1: Second-order compact splitting Fourier spectral method

Input: Initial data Ψ^n and time step τ .

- 1: Solve the nonlinear subproblem by (3.14) for half time step $\tau/2$ with initial data Ψ^n to obtain Ψ^* .
- 2: Solve the linear subproblem for time step τ with the data $\Psi^* = (\psi_2^*, \psi_1^*, \psi_0^*, \psi_{-1}^*, \psi_{-2}^*)^\top$:
 - Compute the mapping $\phi_\ell^n = e^{-i\ell\Omega t} \psi_\ell^*(\mathcal{R}(t_n)\mathbf{x})$ by (3.6).
 - Solve the ODEs (3.3) to obtain ϕ_ℓ^{n+1} using (3.5).
 - Compute the mapping $\psi_\ell^{**} = e^{i\ell\Omega t} \phi_\ell^{n+1}(\mathcal{R}^{-1}(t_{n+1})\mathbf{x})$ by (3.7).
- 3: Solve the nonlinear subproblem by (3.14) for half time step $\tau/2$ with the data $\Psi^{**} = (\psi_2^{**}, \dots, \psi_{-2}^{**})^\top$ to obtain the final solution Ψ^{n+1} .

Output: Numerical solution Ψ^{n+1} .

Remark 3.5 (Efficiency). *In Algorithm 1, we can reduce the number of Fourier-Physical switches by merging adjacent computation. As a result, only $30N$ pairs of one-dimensional FFTs and iFFTs are required in step 2, and the complexity is $O(N^2 \log N)$. For the 3D case, the schemes requires $35N^2$ pairs of one-dimensional FFTs and iFFTs, and the complexity becomes $O(N^3 \log N)$.*

3.4. Stability

In this subsection, we prove that the proposed method preserves the conservation of both mass and magnetization at the discrete level. Without loss of generality, we present proofs in the 2D case and extension to 3D is straightforward. We define the discrete l^2 -norm of ψ_ℓ^n as $\|\psi_\ell^n\|_{l^2} = (h^2 \sum_{j=0}^{N-1} \sum_{k=0}^{N-1} |\psi_{\ell,jk}^n|^2)^{\frac{1}{2}}$, and define $\|\Psi^n\|_{l^2} := \left(\sum_{\ell=-2}^2 \|\psi_\ell^n\|_{l^2}^2 \right)^{\frac{1}{2}}$.

Lemma 3 (Stability). *The mass $\mathcal{N}(\Psi)$ is conserved at discrete level. In fact, for any $h, \tau > 0$, we have*

$$\|\Psi^n\|_{l^2}^2 = \|\Psi^0\|_{l^2}^2.$$

This reveals that the compact splitting Fourier spectral method is unconditionally stable.

proof 3. *For the nonlinear subproblem (3.9), the exact solution (3.14) can be rewritten as*

$$\Psi^{n+1} = e^{-i\tau \mathcal{B}_1^n} \mathbf{b}^n,$$

where $\mathcal{B}_1^n := (V + (c_0 + c_2/5)\rho^n)I_5 + c_1 \mathbf{F}^n \cdot \mathbf{f}$ and $\mathbf{b}^n := \cos(c_2 S \tau) \Psi^n + \frac{i}{5} \sin(c_2 S \tau) (\frac{\rho^n}{5} \Psi^n - A_{00}{}^n A \bar{\Psi}^n)$. Using $(\mathcal{B}_1^n)^H = \mathcal{B}_1^n$, a simple calculation shows that

$$\|\Psi^{n+1}\|_{l^2}^2 = h^2 \sum_{j=0}^{N-1} \sum_{k=0}^{N-1} \left((\mathbf{b}^n)^H e^{i(\mathcal{B}_1^n)^H \tau} e^{-i\mathcal{B}_1^n \tau} \mathbf{b}^n \right)_{jk} = h^2 \sum_{j=0}^{N-1} \sum_{k=0}^{N-1} (\rho^n)_{jk} = \|\Psi^n\|_{l^2}^2,$$

where $(f^n)_{jk} := f(x_j, y_k, t_n)$. While for the linear subproblem, we only need to consider (3.6), (3.7) and (3.5). Based on Parseval's identity and following the methodology in [23], we have

$$\|\Psi^{n+1}\|_{l^2}^2 = \|\Phi^{n+1}\|_{l^2}^2 = \|\Phi^n\|_{l^2}^2 = \|\Psi^n\|_{l^2}^2. \quad (3.15)$$

This completes the proof.

Lemma 4 (Magnetization conservation). *The magnetization $\mathcal{M}(\Psi)$ is conserved at discrete level when $\gamma = 0$. In fact, for any $h, \tau > 0$, we have*

$$\sum_{\ell=-2}^2 \ell \|\psi_\ell^n\|_{l^2}^2 = \sum_{\ell=-2}^2 \ell \|\psi_\ell^0\|_{l^2}^2.$$

proof 4. For the linear subproblem (3.1), we know that $e^{i\tau Q}$ is a diagonal unitary matrix when $\gamma = 0$, as shown in (3.8). Therefore, it follows from (3.15) that

$$\|\psi_\ell^{n+1}\|_{l^2}^2 = \|\psi_\ell^n\|_{l^2}^2.$$

For the nonlinear subproblem (3.9), with the help of (3.11), we have

$$\partial_t \left(\sum_{\ell=-2}^2 \ell \|\psi_\ell\|_{l^2}^2 \right) = h^2 \sum_{j=0}^{N-1} \sum_{k=0}^{N-1} (\partial_t F_z)_{jk} = 0.$$

This implies that

$$\sum_{\ell=-2}^2 \ell \|\psi_\ell^{n+1}\|_{l^2}^2 = \sum_{\ell=-2}^2 \ell \|\psi_\ell^n\|_{l^2}^2.$$

The proof is completed.

4. Numerical results

In this section, we begin by evaluating the performance of our numerical method through the temporal/spatial accuracies and efficiency test. We then apply it to characterize the dynamical laws, including the conservation of mass, energy, magnetization, along with the evolution of angular momentum expectation and condensate widths. Finally, we investigate some interesting phenomena, such as the effect of SOC on dynamics and the dynamics of the vortex lattice. In the following simulations, the external potential $V(\mathbf{x})$ is chosen as (1.4) with $\gamma_x = \gamma_y = 1$ unless stated otherwise. For convenience, throughout this section we denote the second-order/fourth-order Fourier spectral method as **TS2/TS4**.

4.1. Accuracy confirmation.

In this section, we define the numerical errors as

$$E_\ell^{h,\tau} = \|\psi_\ell^{\text{ref}} - \psi_\ell^{h,\tau}\|_{l^2} / \|\psi_\ell^{\text{ref}}\|_{l^2}, \quad \ell = -2, -1, 0, 1, 2,$$

where ψ_ℓ^{ref} is a high-accuracy reference solution, and $\psi_\ell^{h,\tau}$ is a numerical solution obtained with the time step τ and the spatial mesh size h .

To confirm the temporal convergence, we compute the wave function with a small mesh size $h_0 = 2^{d-7}$, and the reference solution ψ_ℓ^{ref} is obtained by TS4 with mesh size h_0 and a small time step $\tau_0 = 10^{-4}$. To confirm the spatial convergence, we compute the wave function with different mesh size h and the reference solution is obtained by TS2/TS4 with h_0 and τ_0 .

Example 1 (Accuracy). *In this example, we test the temporal and spatial accuracy in both 2D and 3D cases. To this end, We consider the following two cases*

- **2D case** : $c_0 = 100$, $c_1 = -1$, $c_2 = 1$, $\Omega = 0.2$, $\gamma = 0.3$.
- **3D case** : $c_0 = 10$, $c_1 = -1$, $c_2 = 1$, $\Omega = 0.2$, $\gamma = 0.1$.

The initial functions are

$$\psi_{\pm 2}^0(\mathbf{x}) = \phi(\mathbf{x}), \quad \psi_{\pm 1}^0(\mathbf{x}) = \phi(\mathbf{x}), \quad \psi_0^0(\mathbf{x}) = 2\phi(\mathbf{x}), \quad (4.1)$$

where $\phi(\mathbf{x}) = e^{-|\mathbf{x}|^2/2} / (\sqrt{8}\pi^{d/4})$.

Table 1: Numerical errors of TS2 and TS4 at time $t = 0.5$ for 2D case in **Example 1**.

		τ	1/80	1/160	1/320	1/640
Temporal direction	TS2	$E_2^{h_0, \tau}$	8.4374E-04	2.1064E-04	5.2641E-05	1.3159E-05
		rate		2.0020	2.0005	2.0002
		$E_1^{h_0, \tau}$	8.4254E-04	2.1042E-04	5.2592E-05	1.3147E-05
		rate		2.0015	2.0004	2.0001
		$E_0^{h_0, \tau}$	5.4795E-04	1.3690E-04	3.4222E-05	8.5552E-06
		rate		2.0008	2.0002	2.0001
	TS4	$E_{-1}^{h_0, \tau}$	8.3759E-04	2.0918E-04	5.2282E-05	1.3069E-05
		rate		2.0015	2.0004	2.0001
		$E_{-2}^{h_0, \tau}$	8.3704E-04	2.0896E-04	5.2224E-05	1.3054E-05
		rate		2.0020	2.0005	2.0001
		$E_2^{h_0, \tau}$	4.1380E-05	2.6390E-06	1.6583E-07	1.0379E-08
		rate		3.9708	3.9922	3.9980
		$E_1^{h_0, \tau}$	3.4689E-05	2.2035E-06	1.3833E-07	8.6550E-09
		rate		3.9766	3.9937	3.9984
Spatial direction	TS2	$E_0^{h_0, \tau}$	2.1960E-05	1.3992E-06	8.7900E-08	5.2021E-09
		rate		3.9722	3.9925	3.9978
		$E_{-1}^{h_0, \tau}$	3.4512E-05	2.1923E-06	1.3762E-07	8.6109E-09
		rate		3.9766	3.9937	3.9984
		$E_{-2}^{h_0, \tau}$	4.0945E-05	2.6112E-06	1.6408E-07	1.0269E-08
	rate		3.9709	3.9922	3.9980	
	TS4	h	1/2	1/4	1/8	1/16
		E_2^{h, τ_0}	2.1323E-01	3.2161E-03	4.5656E-08	1.3003E-12
		E_1^{h, τ_0}	2.1990E-01	3.4138E-03	3.8468E-08	1.2759E-12
		E_0^{h, τ_0}	1.7801E-01	2.3852E-03	3.5863E-08	1.3317E-12
E_{-1}^{h, τ_0}		2.2702E-01	3.5795E-03	4.2493E-08	1.2192E-12	
E_{-2}^{h, τ_0}		2.1287E-01	3.4759E-03	5.0031E-08	1.2682E-12	
TS4		E_2^{h, τ_0}	2.1323E-01	3.2161E-03	4.5658E-08	3.7094E-12
		E_1^{h, τ_0}	2.1990E-01	3.4138E-03	3.8470E-08	3.5924E-12
		E_0^{h, τ_0}	1.7801E-01	2.3852E-03	3.5864E-08	3.6499E-12
		E_{-1}^{h, τ_0}	2.2702E-01	3.5795E-03	4.2494E-08	3.3506E-12
	E_{-2}^{h, τ_0}	2.1287E-01	3.4759E-03	5.0032E-08	3.4201E-12	

Table 1 presents the temporal and spatial errors computed by TS2 and TS4 at time $t = 0.5$ on the computational domain $\mathcal{D} = [-12, 12]^2$ for the 2D case, while Table 2 presents those at time $t = 0.3$ on the computational domain $\mathcal{D} = [-8, 8]^3$ for the 3D case. Tables 1-2 demonstrate that TS2/TS4 achieves second/fourth order accuracy in time and exhibits spectral accuracy in space. Furthermore, a higher order operator splitting scheme is made possible owing to the exact integrability of both subproblems.

Table 2: Numerical errors of TS2 and TS4 at time $t = 0.3$ for 3D case in **Example 1**.

		τ	1/40	1/80	1/160	1/320
Temporal direction	TS2	$E_2^{h_0, \tau}$	7.3666E-05	1.8405E-05	4.6005E-06	1.1501E-06
		rate	*	2.0009	2.0002	2.0001
		$E_1^{h_0, \tau}$	4.5933E-05	1.1477E-05	2.8688E-06	7.1718E-07
		rate	*	2.0008	2.0002	2.0001
		$E_0^{h_0, \tau}$	6.9868E-05	1.7456E-05	4.3633E-06	1.0908E-06
		rate	*	2.0009	2.0002	2.0001
		$E_{-1}^{h_0, \tau}$	4.5752E-05	1.1432E-05	2.8575E-06	7.1436E-07
	rate	*	2.0008	2.0002	2.0001	
	$E_{-2}^{h_0, \tau}$	7.3626E-05	1.8395E-05	4.5980E-06	1.1495E-06	
	rate	*	2.0009	2.0002	2.0001	
	TS4	$E_2^{h_0, \tau}$	5.8017E-07	3.7139E-08	2.3356E-09	1.4621E-10
		rate	*	3.9655	3.9911	3.9976
		$E_1^{h_0, \tau}$	3.2720E-07	2.1001E-08	1.3215E-09	8.2668E-11
		rate	*	3.9617	3.9902	3.9987
$E_0^{h_0, \tau}$		5.5258E-07	3.5367E-08	2.2241E-09	1.3925E-10	
rate		*	3.9657	3.9911	3.9975	
$E_{-1}^{h_0, \tau}$		3.2671E-07	2.0969E-08	1.3195E-09	8.2570E-11	
rate	*	3.9617	3.9902	3.9983		
$E_{-2}^{h_0, \tau}$	5.8010E-07	3.7134E-08	2.3353E-09	1.4621E-10		
rate	*	3.9655	3.9911	3.9975		
		h	1	1/2	1/4	1/8
Spatial direction	TS2	E_2^{h, τ_0}	1.5025E-02	2.1334E-04	8.0943E-10	5.0698E-13
		E_1^{h, τ_0}	1.0510E-02	8.4964E-05	3.9352E-10	4.9918E-13
		E_0^{h, τ_0}	1.4270E-02	2.0077E-04	7.5453E-10	5.0477E-13
		E_{-1}^{h, τ_0}	1.0646E-02	8.1368E-05	3.7883E-10	5.1567E-13
		E_{-2}^{h, τ_0}	1.5169E-02	2.1555E-04	8.0559E-10	5.1528E-13
	TS4	E_2^{h, τ_0}	1.5025E-02	2.1334E-04	8.1061E-10	1.5136E-12
		E_1^{h, τ_0}	1.0510E-02	8.4964E-05	3.9306E-10	1.5238E-12
		E_0^{h, τ_0}	1.4270E-02	2.0077E-04	7.5567E-10	1.5391E-12
		E_{-1}^{h, τ_0}	1.0646E-02	8.1368E-05	3.7846E-10	1.5625E-12
		E_{-2}^{h, τ_0}	1.5169E-02	2.1555E-04	8.0677E-10	1.5388E-12

4.2. Efficiency test

In this subsection, we compare the computational costs of our method and that proposed in [23]. In addition, we illustrate the efficiency of our numerical method by characterizing the functional relationship between the computational costs and the discrete problem size. For convenience, we denote our method as **M1** and the reference method as **M2**.

Example 2 (Efficiency). *In this example, we test the computational costs for different total grid number $N_{tot} := N^d$ in both 2D and 3D cases, using M1 and M2 method. We set the parameters $c_0 = 10$, $c_1 = 1$, $c_2 = 1$, $\Omega = 0.2$, $\gamma = 0.1$, and the initial condition (4.1). The computational cost is defined as the CPU time(s) consumed to advance the simulations from time $t = 0$ to $t = 0.1$. The simulations were coded in FORTRAN, and executed on the dual-socket 3.00GHz Intel(R) Xeon(R) Gold 6248R CPUs with a 35.75 MB L3 cache in Ubuntu 18.04.6 LTS with the Intel compiler ifort.*

Table 3 presents the computational costs obtained by the M1 method using TS2 and TS4 with a time step $\tau = 10^{-3}$ on the computational domain $\mathcal{D} = [-12, 12]^d$, for various total grid sizes N_{tot} in both 2D and

Table 3: Timing results (in seconds) with the total grid number N_{tot} by M1 method for d -dimensional cases in **Example 2**.

	N_{tot}	64^d	128^d	192^d	256^d
$d = 2$	TS2	0.68	2.99	8.12	17.77
	TS4	1.57	7.02	18.03	40.71
$d = 3$	TS2	75.22	622.01	2449.06	6137.38
	TS4	172.46	1643.12	5671.32	14688.66

Table 4: Timing results (in seconds) with the total grid number N_{tot} by M2 method for d -dimensional cases in **Example 2**.

	N_{tot}	64^d	128^d	192^d	256^d
$d = 2$	TS2	0.65	2.73	7.04	15.99
	TS4	1.48	6.22	16.12	36.51
$d = 3$	TS2	69.28	564.38	2253.20	5663.66
	TS4	159.21	1516.94	5225.02	13462.51

3D cases. Table 4 reports the corresponding results obtained by the M2 method under the same setting. Figure 1 illustrates the results from Table 4 via Log-Log plots. A comparison between Table 3 and Table 4 exhibits that the computational costs of M2 are less than that of M1, which aligns with Remark 3.2. As shown in Table 4 and Figure 1, the computational cost scales approximately as $O(N_{tot} \log N_{tot})$, which agrees with the theoretical analysis in Remark 3.5 and thus confirms the efficiency of our numerical method.

4.3. Dynamical properties verification.

In this subsection, we apply our numerical method to investigate the dynamical laws, including the conservation of mass, energy, and magnetization, as well as the evolution of angular momentum expectation and condensate widths.

Example 3. *In this example, we numerically characterize the dynamical laws in 2D case. To this end, we take the parameters $c_0 = 120$, $c_1 = 1$, $c_2 = 1$, $\Omega = 0.2$, adopt the harmonic potential $V(\mathbf{x})$ given in (1.4), and consider the following three cases*

- **Case i:** $\gamma_x = \gamma_y = 1$, $\gamma = 0$.
- **Case ii:** $\gamma_x = \gamma_y = 1$, $\gamma = 0.9$.
- **Case iii:** $\gamma_x = 1.3$, $\gamma_y = 1$, $\gamma = 0$.

The initial functions are chosen as

$$\psi_{\pm 2}^0(\mathbf{x}) = \phi(\mathbf{x}), \quad \psi_{\pm 1}^0(\mathbf{x}) = \phi(\mathbf{x}), \quad \psi_0^0(\mathbf{x}) = 6\sqrt{7}\phi(\mathbf{x}), \quad (4.2)$$

where $\phi(\mathbf{x}) = e^{-|\mathbf{x}|^2/8}/(32\sqrt{\pi})$. The computational domain, computational time interval, mesh size and time step are respectively set as $\mathcal{D} = [-24, 24]^2$, $t \in [0, 12]$, $h = 1/16$ and $\tau = 10^{-3}$.

Figure 2-3 present the time evolution of mass $\mathcal{N}(t)$, energy $\mathcal{M}(t)$, magnetization $\mathcal{M}(t)$, $\mathcal{E}(t)/\mathcal{E}(0) - 1$, and $\mathcal{E}_{n+1} - \mathcal{E}_n$. Figure 2 demonstrates the conservation of mass, as well as the conservation of magnetization under the condition $\gamma = 0$. Furthermore, Figure 2-3 show that energy is approximately conserved with high accuracy at the discrete level. Figure 4 presents the evolution of the angular momentum expectation $\langle L_z \rangle(t)$ and the $\delta_\nu(t)$ ($\nu = x, y, r$). Figure 4 shows that under the condition about radially symmetric harmonic potential and $\gamma = 0$, the angular momentum expectation is conserved and δ_r is periodic. Furthermore, we observe that $\delta_x = \delta_y = \frac{1}{2}\delta_r$ for radially symmetric initial data.

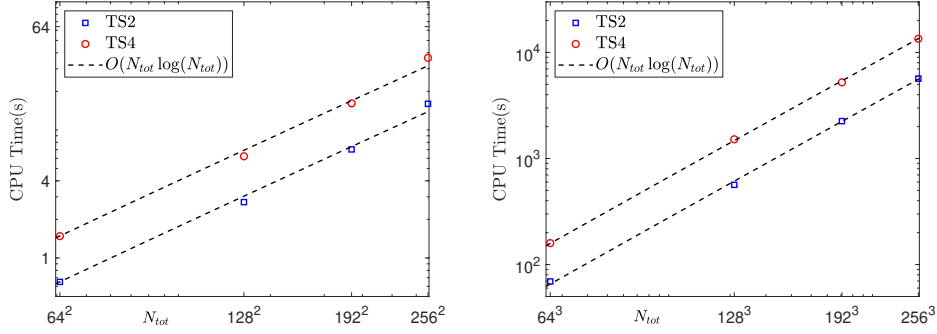


Figure 1: Log-Log plots of timing results with the total grid N_{tot} by TS2 and TS4 for both 2D (left) and 3D (right) cases in **Example 2**.

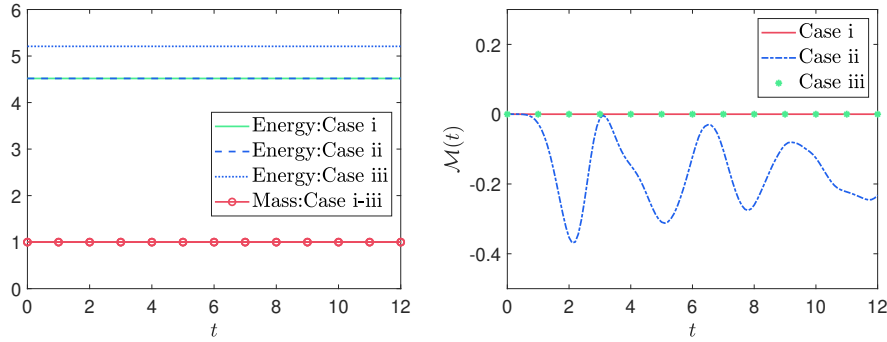


Figure 2: Evolution of mass $\mathcal{N}(t)$ and energy $\mathcal{E}(t)$ (left) and magnetization $\mathcal{M}(t)$ (right) for Case i-Case iii in **Example 3**.

4.4. SOC effects.

In this subsection, we investigate the effects of SOC on dynamics in rotating spin-orbit coupled spin-2 BECs.

Example 4. In the example, we investigate the SOC effects in 2D case. To this end, we take the parameters $c_0 = 243$, $c_1 = 12.1$, $c_2 = -13$ [10, 28], $\Omega = 0.2$, and choose different value of the spin-orbit coupling strength γ . Regarding the initial functions, we consider the following two cases

- **Case i:** $\psi_{\pm 2}^0(\mathbf{x}) = \phi(\mathbf{x})$, $\psi_{\pm 1}^0(\mathbf{x}) = \phi(\mathbf{x})$, $\psi_0^0(\mathbf{x}) = 6\sqrt{7}\phi(\mathbf{x})$.
- **Case ii:** $\psi_{\pm 2}^0(\mathbf{x}) = \phi(\mathbf{x})(x + iy)$, $\psi_{\pm 1}^0(\mathbf{x}) = \phi(\mathbf{x})$, $\psi_0^0(\mathbf{x}) = 6\sqrt{7}\phi(\mathbf{x})(x + iy)$,

where $\phi(\mathbf{x}) = e^{-|\mathbf{x}|^2/2} / (16\sqrt{\pi})$.

Figure 5-6 show contour plots of the densities with different γ at time $t = 1$ for Case i-ii respectively, computed using TS2 with mesh size $h = 1/16$ and time step $\tau = 10^{-3}$ on the computational domain $\mathcal{D} = [-24, 24]^2$. These figures demonstrate that spin-orbit coupling interaction can generate spatial spin structures [18].

4.5. Dynamics of a vortex lattice.

In this subsection, we investigate the dynamics of the vortex lattice in rotating spin-orbit coupled spin-2 BECs.

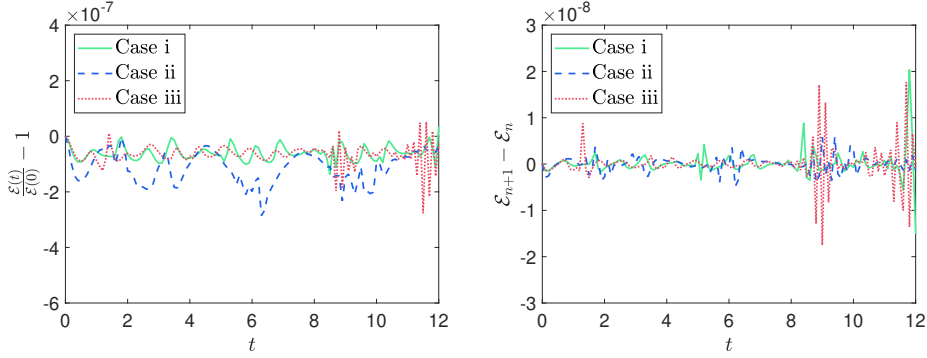


Figure 3: Evolution of $\frac{\varepsilon(t)}{\varepsilon(0)} - 1$ (left) and $\varepsilon_{n+1} - \varepsilon_n$ (right) for Case i-Case iii in **Example 3**.

Example 5. In this example, we choose the parameters $c_0 = 243$, $c_1 = 12.1$, $c_2 = -13$, $\Omega = 0.8$, $\gamma = 2$, and a trapping potential (1.4) with $\gamma_x = \gamma_y = 1$. The initial condition is taken as a stationary vortex state, computed via the preconditioned conjugate gradient method under the conditions specified above. Then we investigate the dynamics of vortex lattice through the following two cases

- **Case i :** The spin-orbit coupling strength is increased to $\gamma = 4$.
- **Case ii :** The external potential is made anisotropic with $\gamma_x = 0.9$ and $\gamma_y = 1.1$.

Figure 7-8 depict contour plots of the densities with different time t for Case i-ii respectively, computed using TS2 with grid point number $N = 256$ and time step $\tau = 10^{-3}$ on the computational domain $\mathcal{D} = [-18, 18]^2$. From Figure 7, we can observe that the vortex lattice undergoes rotation and contraction as γ increases. Additionally, Figure 8 shows that under the anisotropic external potential, the condensates expand along the x -direction and compress along the y -direction over time, leading to the formation of a sheet-like vortex lattice [7, 13].

5. Conclusion

We presented efficient high-order numerical schemes to simulate the dynamics of rotating SOC spin-2 BECs. The Hamiltonian is split into a linear part \mathcal{A} (comprising the Laplace, rotation, and SOC terms) and a nonlinear part \mathcal{B} (consisting of all remaining terms). We integrate the linear subproblem exactly and explicitly in phase space through a function mapping, which transforms the equation into an autonomous evolution equation without rotation term. This mapping The nonlinear subproblem is integrated analytically in physical space as usual. This compact splitting facilitates the design of high-order Fourier spectral method. Our method is spectrally accurate in space and high order in time. It is explicit, unconditionally stable, and conserves the mass and magnetization (when $\gamma = 0$) at discrete level. The dynamical laws of total mass, energy, magnetization, angular momentum expectation and condensate widths are also derived and confirmed numerically. Moreover, our method can be easily adapted and extended to simulate other rotating systems, such as the rotating SOC spin-3 BECs with/without dipole-dipole interactions.

Acknowledgements

This work was partially supported by the National Natural Science Foundation of China No. 11971007 (Y. Yuan), No. 12271400, the National Key R&D Program of China No. 2024YFA1012803 and basic research fund of Tianjin University under grant 2025XJ21-0010 (X. Liu and Y. Zhang).

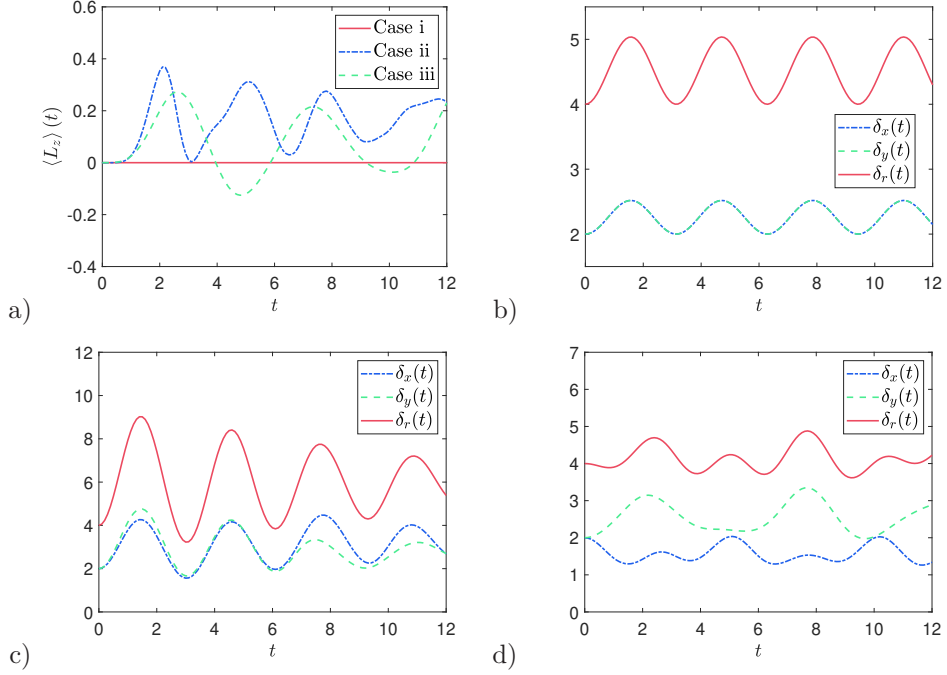


Figure 4: Evolution of angular momentum expectation $\langle L_z \rangle(t)$ (a) and condensate widths (b)-(d) for Case i-Case iii in Example 3.

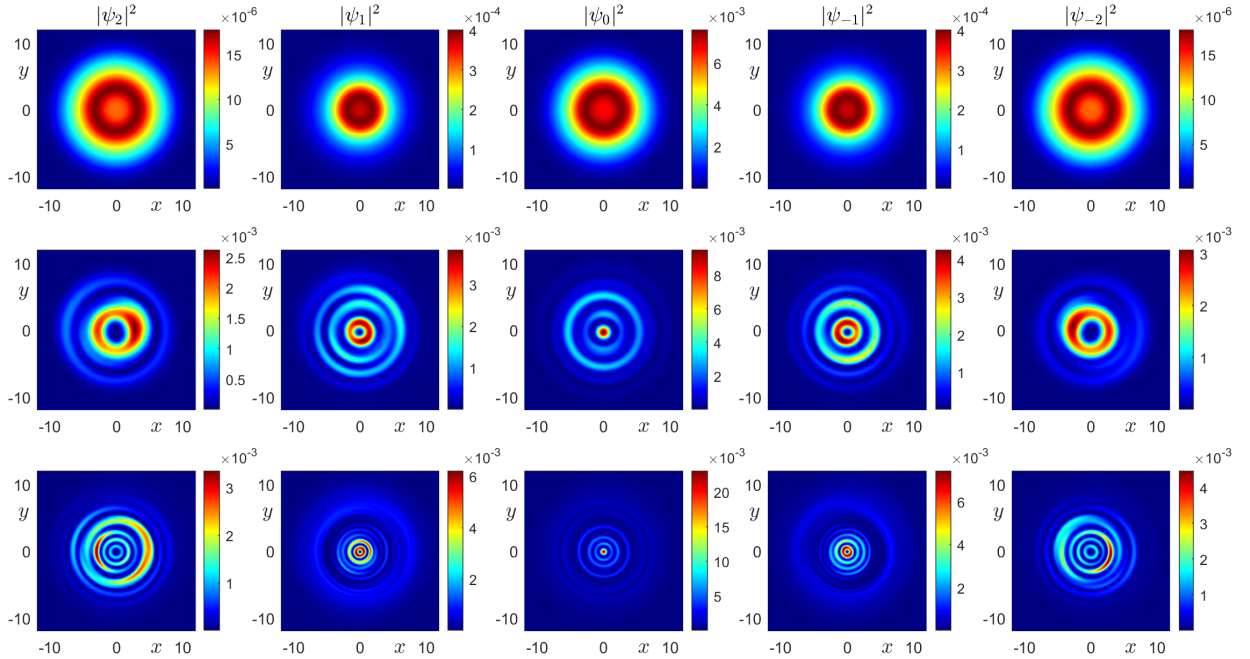


Figure 5: Contour plots of the densities with $\gamma = 0, 0.7, 2$ (top to bottom) in Case i of Example 4.

References

- [1] M. H. Anderson, J. R. Ensher, M. R. Matthews, C. E. Wieman, E. A. Cornell, Observation of Bose-Einstein condensation in a dilute atomic vapor, Science 269 (1995) 198-201.

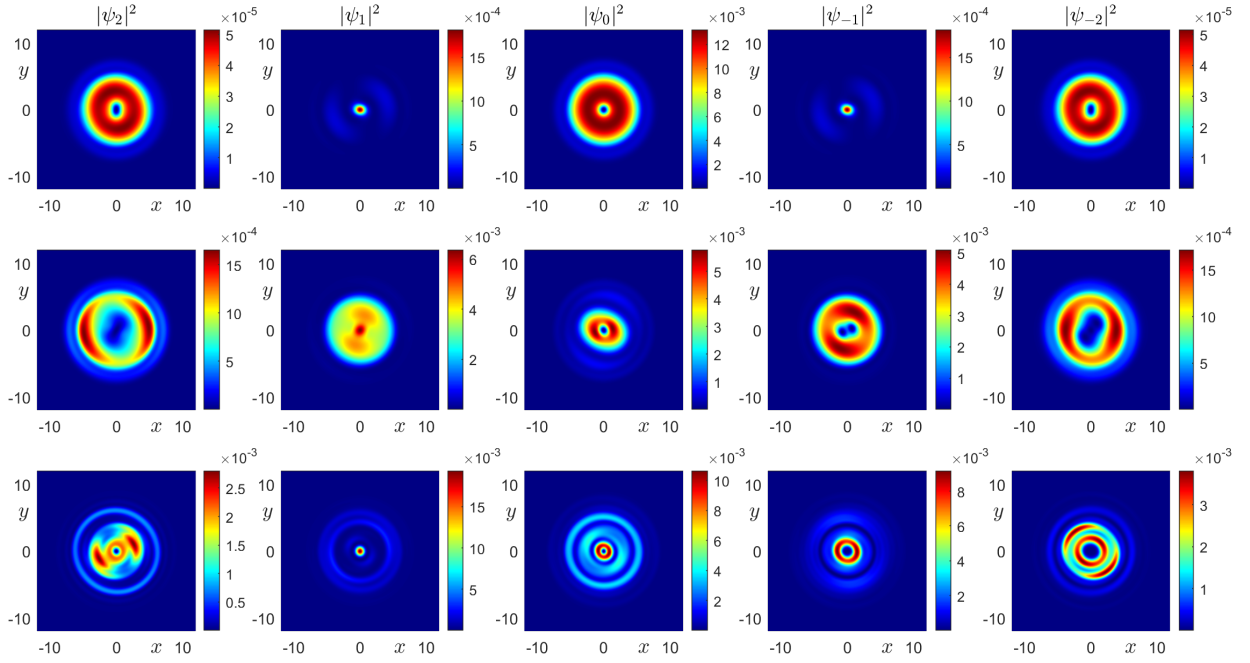


Figure 6: Contour plots of the densities with $\gamma = 0, 0.3, 1.2$ (top to bottom) in Case ii of **Example 4**.

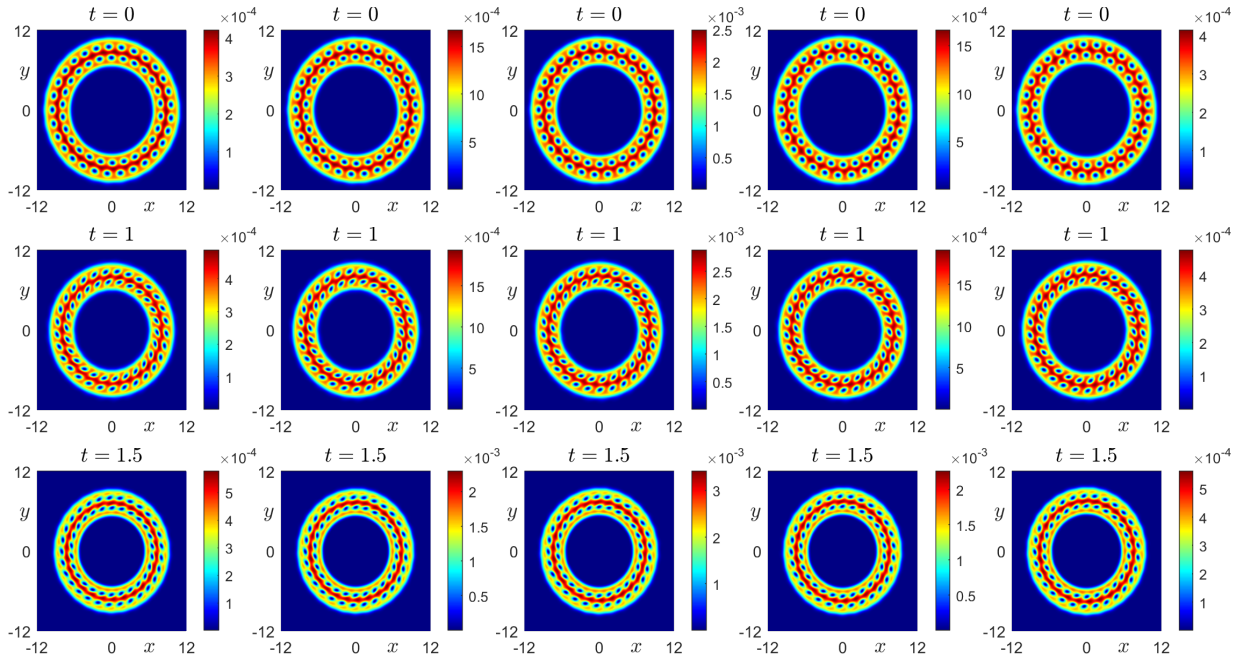


Figure 7: Contour plots of $|\psi_\ell|^2$ ($\ell = 2, 1, 0, -1, -2$, from left to right) for Case i in **Example 5**.

- [2] X. Antoine, W. Bao, C. Besse, Computational methods for the dynamics of the nonlinear Schrödinger/Gross-Pitaevskii equations, *Comput. Phys. Comm.* 184 (2013) 2621-2633.
- [3] W. Bao, Y. Cai, Mathematical theory and numerical methods for Bose-Einstein condensation, *Kinet. Relat. Models* 6 (2013) 1-135.

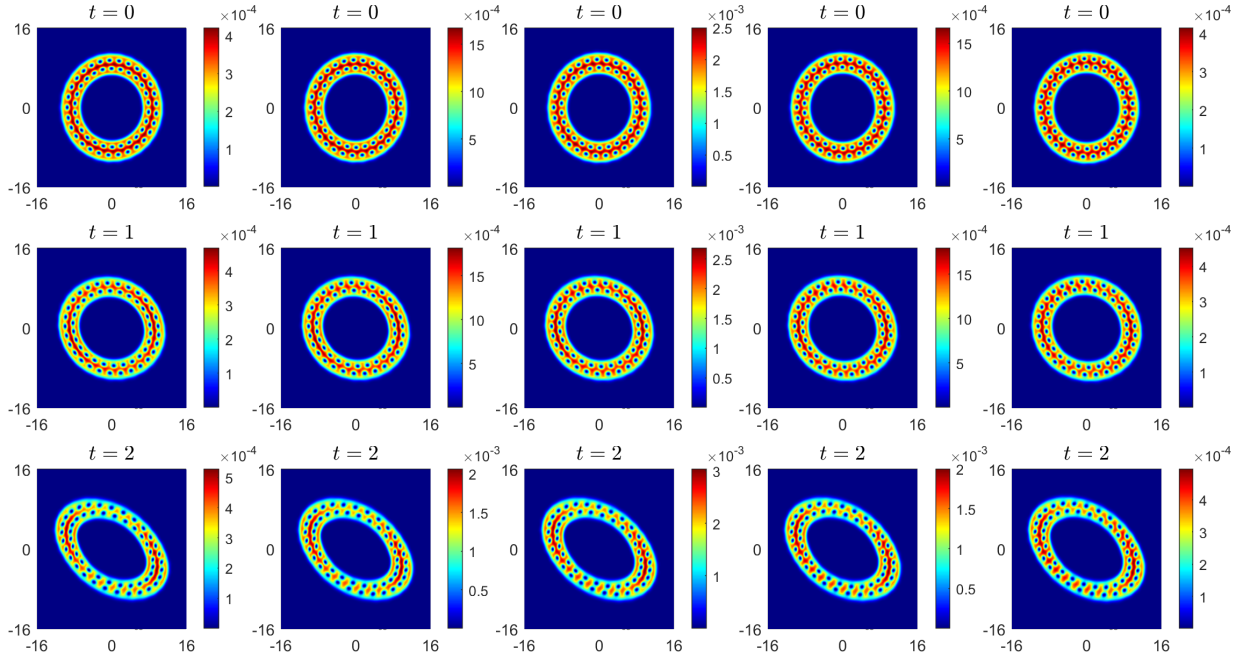


Figure 8: Contour plots of $|\psi_\ell|^2$ ($\ell = 2, 1, 0, -1, -2$, from left to right) for Case ii in **Example 5**.

- [4] W. Bao, Y. Cai, Mathematical models and numerical methods for spinor Bose-Einstein condensates, *Commun. Comput. Phys.* 24 (2018) 899-965.
- [5] W. Bao, D. Jaksch, P. A. Markowich, Numerical solution of the Gross-Pitaevskii equation for Bose-Einstein condensation, *J. Comput. Phys.* 187 (2003) 318-342.
- [6] W. Bao, D. Marahrens, Q. Tang, Y. Zhang, A simple and efficient numerical method for computing the dynamics of rotating Bose-Einstein condensates via rotating Lagrangian coordinates, *SIAM J. Sci. Comput.* 35 (2013) A2671-A2695.
- [7] W. Bao, H. Wang, An efficient and spectrally accurate numerical method for computing dynamics of rotating Bose-Einstein condensates, *J. Comput. Phys.* 217 (2006) 612-626.
- [8] W. Bao, Y. Zhang, Dynamics of the ground state and central vortex states in Bose-Einstein condensation, *Math. Models Methods Appl. Sci.* 15 (2005) 1863-1896.
- [9] P. Banger, P. Kaur, Arko Roy, S. Gautam, FORTRESS: FORTRAN programs to solve coupled Gross-Pitaevskii equations for spin-orbit coupled spin-f Bose-Einstein condensate with spin f=1 or 2, *Comp. Phys. Comm.* 279 (2022) 108442.
- [10] Y. Cai, W. Liu, Efficient and accurate gradient flow methods for computing ground states of spinor Bose-Einstein condensates, *J. Comput. Phys.* 433 (2011) 110183.
- [11] M. M. Cerimele, M. L. Chiofalo, F. Pistella, S. Succi, M. P. Tosi, Numerical solution of the Gross-Pitaevskii equation using an explicit finite-difference scheme: An application to trapped Bose-Einstein condensates, *Phys. Rev. E* 62 (2000) 1382-1389.
- [12] X. Chen, Y. Yuan, Y. Zhang, An efficient time-splitting method to simulate the dynamics of spin-orbit coupled spin-1 Bose-Einstein condensates, *Commun. Comput. Phys.* 39(2026) 119-146.
- [13] P. Engels, I. Coddington, P.C. Haljan, E.A. Cornell, Nonequilibrium effects of anisotropic compression applied to vortex lattices in Bose-Einstein condensates, *Phys. Rev. Lett.* 89 (2002) 100403.

- [14] M. Z. Hasan, C. L. Kane, Colloquium: Topological insulators, *Rev. Mod. Phys.* 82 (2010) 3045-3067.
- [15] A. Ji, W. Liu, J. Song, F. Zhou, Dynamical creation of fractionalized vortices and vortex lattices, *Phys. Rev. Lett.* 101 (2008) 010402.
- [16] Y. K. Kato, R. C. Myers, A. C. Gossard, D. D. Awschalom, Observation of the spin Hall effect in semiconductors, *Science* 306 (2004) 1910-1913.
- [17] P. Kaur, Arko Roy, S. Gautam, FORTRESS: FORTRAN programs for solving coupled Gross-Pitaevskii equations for spin-orbit coupled spin-1 Bose-Einstein condensate, *Comp. Phys. Comm.* 259 (2021) 107671.
- [18] Y. Kawaguchi, M. Ueda, Spinor Bose-Einstein condensates, *Phys. Rep.* 520 (2012) 253-381.
- [19] J. D. Koralek, C. P. Weber, J. Orenstein, B. A. Bernevig, S. C. Zhang, S. Mack, D. D. Awschalom, Emergence of the persistent spin helix in semiconductor quantum wells, *Nature* 458 (2009) 610-613.
- [20] R. Liao, Y. Yu, W. Liu, Tuning the tricritical point with spin-orbit coupling in polarized Fermionic condensates, *Phys. Rev. Lett.* 108 (2012) 080406.
- [21] Y. J. Lin, K. Jiménez-García, I. B. Spielman, Spin-orbit-coupled Bose-Einstein condensates, *Nature* 471 (2011) 83-86.
- [22] X. Liu, X. Meng, Q. Tang, Y. Zhang, High-order compact splitting spectral methods for the rotating spin-1 Bose-Einstein condensates in a magnetic field, *Math. Models Methods Appl. Sci.* 35 (2025) 2013-2045.
- [23] X. Liu, Y. Yuan, Y. Zhang, An efficient compact splitting Fourier spectral method for computing the dynamics of rotating spin-orbit coupled spin-1 Bose-Einstein condensates, *J. Comput. Phys.* 529 (2025) 113892.
- [24] P. Muruganandam, S. K. Adhikari, Fortran programs for the time-dependent Gross-Pitaevskii equation in a fully anisotropic trap, *Comput. Phys. Commun.* 180 (2009) 1888-1912.
- [25] J. Shen, T. Tang, L. Wang, *Spectral Methods: Algorithms, Analysis and Applications*, Springer, 2011.
- [26] D. M. Stamper-Kurn, M. R. Andrews, A. P. Chikkatur, S. Inouye, H.-J. Miesner, J. Stenger, W. Ketterle, Optical confinement of a Bose-Einstein condensate, *Phys. Rev. Lett.* 80 (1998) 2027-2030.
- [27] L. M. Symes, P. B. Blakie, Solving the spin-2 Gross-Pitaevskii equation using exact nonlinear dynamics and symplectic composition, *Phys. Rev. E* 95 (2017) 013311.
- [28] T. Tian, Y. Cai, X. Wu, Z. Wen, Ground States of Spin-F Bose-Einstein Condensates, *SIAM J. Sci. Comput.* 42 (2020) B983-B1013.
- [29] R. P. Tiwari, A. Shukla, A basis-set based Fortran program to solve the Gross-Pitaevskii equation for dilute Bose gases in harmonic and anharmonic traps, *Comput. Phys. Comm.* 174 (2006) 966-982.
- [30] J. Wang, W. Wang, S. Yang, Classifying the ground-state phases of spin-orbit coupled spin-2 Bose-Einstein condensate in momentum space, *Phys. Lett. A* 383 (2019) 566-569.
- [31] F. Wilczek, Majorana returns, *Nat. Phys.* 5 (2009) 614-618.
- [32] L. Xu, Y. Liu, S. Feng, S. Yang, Fractional spin-vortex states in $F = 2$ spinor Bose-Einstein condensates, *Phys. Lett. A* 383 (2019) 2515-2518.
- [33] H. Yoshida, Construction of higher order symplectic integrators, *Phys. Lett. A* 150 (1990) 262-268.

- [34] D. Zhang, T. Gao, P. Zou, L. Kong, R. Li, X. Shen, X. Chen, S. Peng, M. Zhan, H. Pu, K. Jiang, Ground-state phase diagram of a spin-orbital-angular-momentum coupled Bose-Einstein condensate, *Phys. Rev. Lett.* 122 (2019) 110402.
- [35] X. Zhang, B. Li, S. Zhang, Rotating spin-orbit coupled Bose-Einstein condensates in concentricly coupled annular traps, *Laser Phys.* 23 (2013) 105501.
- [36] X. Zhou, J. Zhou, C. Wu, Vortex structures of rotating spin-orbit-coupled Bose-Einstein condensates, *Phys. Rev. A* 84 (2011) 063624.
- [37] H. Zhu, C. Liu, D. Wang, S. Yin, L. Zhuang, W. Liu, Spin-orbit coupling controlling the topological vortical phase transition in spin-2 rotating Bose-Einstein condensates, *Phys. Rev. A* 104(2021) 053325.